Cooperative sensing of mitochondrial DNA by ZBP1 and cGAS promotes cardiotoxicity

Yuanjiu Lei[1], **Jordyn J. VanPortfliet**[1,10], **Yi-Fan Chen**[1,10], **Joshua D. Bryant**[1], **Ying Li**[2], **Danielle Fails**[3], **Sylvia Torres-Odio**[1], **Katherine B. Ragan**[4], **Jingti Deng**[5], **Armaan Mohan**[5], **Bing Wang**[2], **Olivia N. Brahms**[6], **Shawn D. Yates**[6], **Michael Spencer**[3], **Carl W. Tong**[7], **Marcus W. Bosenberg**[8], **Laura Ciaccia West**[1], **Gerald S. Shadel**[9], **Timothy E. Shutt**[5], **Jason W. Upton**[6], **Pingwei Li**[2], **A. Phillip West**[1,11,*]

[1]Department of Microbial Pathogenesis and Immunology, School of Medicine, Texas A&M University, Bryan, TX 77807, USA

[2]Department of Biochemistry and Biophysics, Texas A&M University, College Station, TX 77843, USA

[3]Fortis Life Sciences, Montgomery, TX 77356, USA

[4]Department of Molecular Biosciences, University of Texas at Austin, Austin, TX 78712, USA

[5]Departments of Medical Genetics and Biochemistry & Molecular Biology, Cumming School of Medicine, University of Calgary, Calgary, AB T2N 1N4, Canada

[6]Department of Biological Sciences, Auburn University, Auburn, AL 36849, USA

[7]Department of Medical Physiology, School of Medicine, Texas A&M University, Bryan, TX 77807, USA

[8]Departments of Pathology, Dermatology, and Immunobiology, Yale School of Medicine, New Haven, CT 06520, USA

[9]Salk Institute for Biological Studies, La Jolla, CA 92037, USA

[10]These authors contributed equally

[11]Lead contact

SUMMARY

Mitochondrial DNA (mtDNA) is a potent agonist of the innate immune system; however, the exact immunostimulatory features of mtDNA and the kinetics of detection by cytosolic nucleic acid sensors remain poorly defined. Here, we show that mitochondrial genome instability promotes Z-form DNA accumulation. Z-DNA Binding Protein 1 (ZBP1) stabilizes Z-form mtDNA and nucleates a cytosolic complex containing cGAS, RIPK1, and RIPK3 to sustain STAT1 phosphorylation and type I interferon (IFN-I) signaling. Elevated Z-form mtDNA, ZBP1 expression, and IFN-I signaling are observed in cardiomyocytes after exposure to Doxorubicin, a first-line chemotherapeutic agent that induces frequent cardiotoxicity in cancer patients. Strikingly, mice lacking ZBP1 or IFN-I signaling are protected from Doxorubicin-induced cardiotoxicity. Our findings reveal ZBP1 as a cooperative partner for cGAS that sustains IFN-I responses to mitochondrial genome instability and highlight ZBP1 as a potential target in heart failure and other disorders where mtDNA stress contributes to interferon-related pathology.

Graphical Abstract
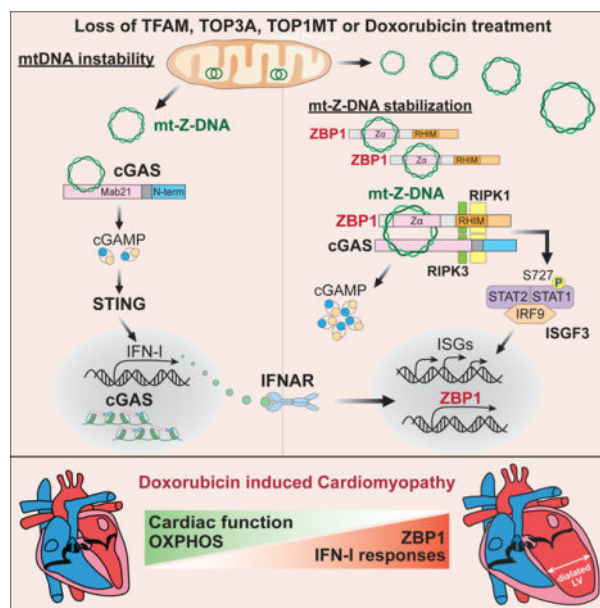
In Brief

Coordinated interaction of the ZBP1 and cGAS pathways tie sensing of mitochondrial Z-DNA to type I interferon signaling and cardiac damage.

INTRODUCTION

Under conditions of cellular stress and mitochondrial dysfunction, mtDNA can be released into the cytoplasm or extracellular space to engage pattern recognition receptors (PRRs) including Toll-like receptor 9 (TLR9), NOD-like receptor family pyrin domain containing 3 (NLRP3), cyclic GMP-AMP (cGAMP) synthase (cGAS), and ZBP1[1–6]. The detection of mtDNA can potentiate antimicrobial innate immunity during infection but may also drive detrimental inflammatory responses in disease and aging[7,8]. Despite growing evidence that mtDNA is an important innate immune agonist, many questions remain. Notably, the

physiological and pathological contexts of mtDNA release and the molecular properties of mtDNA that stabilize it in the cytosol and enhance detection by cGAS or other innate immune sensors have not been fully elucidated.

As a covalently closed, circular genome, mtDNA lacks free DNA ends that can rotate to relieve torsional strain induced during replication and transcription[9]. Consequently, the activity of mitochondrial replication and transcription machineries can generate overwound (positively supercoiled) and underwound (negatively supercoiled) regions of mtDNA, which may promote the formation of other immunostimulatory mtDNA structures if not properly resolved. Z-DNA is one such non-canonical structure that differs from canonical Watson-Crick B-DNA[10,11]. Sequences with alternating purine-pyrimidine regions have the highest propensity to form Z-DNA, although negative supercoiling of other sequences can promote B to Z transition[12,13]. In mitochondria, the activity of DNA topoisomerase I mitochondrial (TOP1MT) and DNA topoisomerase III alpha (TOP3A) are required to relieve torsional mtDNA stress and relax negative supercoiling[9,11]. However, the degree to which torsional stress promotes B- to Z-DNA transition in mtDNA is unknown, and whether the acquisition of this unique DNA confirmation enhances or sustains the immunostimulatory potential of mtDNA is presently unclear. Emerging evidence suggests ZBP1 is a critical innate immune receptor for both nuclear Z-DNA and double stranded Z-RNA[14–22], yet a role for ZBP1 in sensing Z-form mtDNA has not been explored.

DNA damage is a main mechanism by which Doxorubicin (Doxo) and other anthracycline chemotherapeutics induce cancer cell death[23]. Unfortunately, Doxo has many adverse effects on the cardiovascular system and can cause acute cardiotoxicity, cardiomyopathy, and heart failure in cancer patients and survivors[24–28]. Mitochondrial dysfunction and mtDNA instability are strongly linked to Doxo-induced cardiotoxicity (DIC)[23,29–33]. Notably, mice lacking TOP1MT are more susceptible to Doxo-induced mtDNA damage and cardiac dysfunction[34]. Doxo also induces mtDNA supercoiling[35], suggesting that increased torsional strain or accumulation of non-canonical structures might underlie cardiac mtDNA instability in DIC. Finally, Doxo can trigger the release of mtDNA into the cytoplasm to activate cell-autonomous innate immune signaling through cGAS[36]. The cGAS-STING axis is increasingly implicated in cardiovascular diseases and heart failure[8,37–41], raising the intriguing possibility that Doxo-induced mtDNA stress contributes to DIC via activation of cGAS or other nucleic acid sensing PRRs such as ZBP1.

In this study, we report that ZBP1 is a key innate immune sensor of torsional mtDNA stress and mitochondrial Z-DNA release. We find that ZBP1 stabilizes Z-form mtDNA and nucleates the assembly of a cytosolic complex containing cGAS, receptor-interacting protein 1 (RIPK1), and RIPK3 to engage robust IFN-I signaling. Ablation of ZBP1 or IFN-I signaling limits cardiotoxicity and improves heart function after in vivo Doxo administration, shedding new light on the immune mechanisms of DIC and revealing a potential therapeutic avenue for cancer therapy-associated heart failure.

RESULTS

ZBP1 is required for maximal IFN-I induction downstream of mtDNA stress

Our prior work revealed persistent mitochondrial genome instability, cytosolic mtDNA release (Figure S1A), cGAS-STING signaling, and IFN-I responses (Figure 1) in TFAM heterozygous knockout cells (*Tfam*^{+/−})[42]. Analysis of RNA-seq data from *Tfam*^{+/−} mouse embryonic fibroblasts (MEFs) revealed elevated expression of multiple IFN-I-induced nucleic acid sensors including ZBP1, IFI200 family members, and mitochondrial antiviral signaling (MAVS)-dependent RNA helicases (Figures 1A and S1B). In contrast to *Sting*^{−/−} cells, *Mavs*^{−/−} MEFs maintained high levels of ISGs after TFAM silencing (Figure S1C), indicating that mitochondrial RNA release and sensing is not a major driver of IFN-I signaling in TFAM-deficient cells (Figure S1C). However, silencing of ZBP1 markedly attenuated ISG expression in *Tfam*^{+/−} cells (Figure S1D). Additional analyses confirmed that loss of ZBP1 largely abrogated ISG expression in both TFAM-deficient MEFs (Figures 1A–1C) and human cells (Figure 1D). Experiments in STING-reconstituted 293FT cells (293FT-STING) revealed that co-expression of cGAS and ZBP1 potentiated TFAM depletion-induced ISG expression (Figure 1E). Collectively, these results indicate that ZBP1 is an essential sensor of mtDNA instability that synergizes with cGAS to sustain IFN-I signaling.

Reduced TFAM expression can alter mtDNA topology, promoting the transition from predominantly relaxed monomeric circles to catenated[43] or supercoiled mtDNA species (Figure S1E). The mitochondrial isoform of TOP3A functions to resolve mtDNA catenation and relax negative supercoiling induced during mtDNA replication and transcription[9,11,44,45]. As loss of TOP3A causes mtDNA torsional strain leading to mitochondrial nucleoid aggregation and instability similar to TFAM depletion (Figure 1F)[44], we next investigated whether silencing of TOP3A promotes mtDNA-dependent IFN-I signaling. Interestingly, siRNA knockdown of TOP3A in both mouse and human cells (Figures S1F and S1G) triggered robust ISG expression in a cGAS- and ZBP1-dependent fashion (Figures 1G and 1H). Selective depletion of mtDNA with the chain terminating nucleoside 2',3'-dideoxycytosine (ddC) during TOP3A knockdown revealed that mtDNA, but not nuclear DNA, is the endogenous ligand driving IFN-I responses (Figures S1H and 1I). Mammalian mitochondria also house the type IB topoisomerase TOP1MT, which facilitates mtDNA decatenation by TOP3A and resolves positive and negative mtDNA supercoiling[11,45–47]. Similar to results with TOP3A, knockdown of TOP1MT triggered ISG expression in a cGAS-, ZBP1-, and mtDNA-dependent fashion (Figures S1I–S1L). Collectively, these data indicate that loss of several mitochondrial factors governing mtDNA packaging and topology promotes ISG expression via cGAS and ZBP1.

Doxorubicin is a widely used anthracycline chemotherapeutic drug that induces mtDNA damage and mitochondrial dysfunction, in addition to nuclear DNA damage[23,29]. A recent study revealed that Doxo promotes mtDNA supercoiling and catenation[35], and we observed that Doxo induced mtDNA nucleoid aggregation similar to cells lacking TFAM or TOP3A (Figures 1J). Doxo treatment also promoted cytosolic mtDNA release, as well as upregulation of ZBP1 and other ISGs (Figures S1M–S1O). Moreover, Doxo-induced ISG

expression was independent of MAVS but required mtDNA and signaling via the type I interferon receptor (IFNAR) (Figures S1P–S1R). Doxo-induced ISG expression was also markedly impaired in *Zbp1*^{−/−} cells, similar to TFAM-, TOP3A-, and TOP1MT-deficient cells (Figures 1K and 1L). Pretreatment of *Zbp1*^{−/−} MEFs with interferon beta (IFNβ) before Doxo challenge failed to increase ISGs to the same level as Doxo-treated WT cells, indicating that another IFN-I induced DNA sensor cannot compensate for the loss of ZBP1 (Figure S1S). Finally, experiments in 293FT-STING cells revealed that cGAS and ZBP1 synergize to enhance ISG expression in response to Doxo (Figure 1M). Despite these crucial roles for ZBP1 in promoting IFN-I responses downstream of mtDNA instability, we noted no requirement for ZBP1 in sensing linear B-form immunostimulatory DNA, as reported by several other groups[14,16,48,49] (Figure S1T). Moreover, ZBP1 was not required for cGAS-dependent ISGs triggered by inner mitochondrial membrane (IMM) herniation and caspase inhibition[50–52] (Figure S1U). In sum, these results suggest that ZBP1 is an innate immune sensor of mitochondrial genome instability that augments cGAS-STING dependent IFN-I signaling in human and mouse cells.

ZBP1 stabilizes Z-DNA generated during mtDNA stress

Bidirectional replication and transcription of circular mtDNA generates supercoiling that must be resolved by TOP1MT and TOP3A. This raises the possibility that increased mtDNA supercoiling in TOP3A or TOP1MT deficient cells, and perhaps *Tfam*^{+/−} and Doxo-treated cells, promotes the formation of Z-DNA for detection by ZBP1. To explore this hypothesis, we utilized the Z22 antibody that selectively binds Z-DNA in vitro and in cellulo[53–55]. Gel shift and slot blotting assays confirmed that the Z22 antibody strongly binds plasmid Z-DNA, but not a plasmid with the identical sequence in B-DNA confirmation (Figures 2A, 2B, S2A and S2B). Moreover, the Z22 antibody efficiently labeled Z-DNA in the cell cytoplasm after transfection, but did not immunostain B-DNA, highlighting the utility of this reagent for fluorescent microscopy analysis of Z-DNA (Figure S2C).

Utilizing the Z22 antibody and quantitative immunofluorescence microscopy, we next screened for the presence of Z-DNA in cells experiencing mtDNA stress. Strikingly, we observed increased cytosolic and mitochondrial Z-DNA accumulation in TFAM, TOP3A, and TOP1MT knockdown cells (Figures 2C and 2D). Doxo also enriched Z-DNA in the cytosol and mitochondria as revealed by microscopy and slot blotting (Figures 2E, 2F and S2D), further supporting the notion that perturbations enhancing mtDNA supercoiling promote the accumulation of Z-DNA. Depletion of mtDNA with ddC after silencing of TOP3A or TOP1MT, or Doxo treatment, reduced both mtDNA abundance and aggregation (Figure S2E), while also significantly decreasing overall Z-DNA intensity (Figure S2F), strongly indicating that mtDNA was the source of Z-DNA we observed. However, IMM herniation and caspase inhibition were insufficient in inducing cytosolic or mitochondrial Z-DNA accumulation (Figure S2G). Additional experiments in human cells confirmed increased Z-DNA abundance after TFAM silencing (Figures 2G and 2H). ZBP1 can stabilize Z-form DNA via its Z-DNA binding domains[56–59]. Interestingly, we observed less cytosolic Z-DNA after TFAM, TOP3A, or TOP1MT silencing in *Zbp1*^{−/−}MEFs relative to WT MEFs, with similar trends seen after dual silencing of TFAM and ZBP1 in human cells (Figures 2D, 2G and 2H). Exposure of *Tfam*^{+/−} MEFs to the Z-DNA stabilizer hydralazine[60,61]

dramatically increased overall Z-DNA staining and ISG expression in a ZBP1-dependent fashion (Figures S2H and S2I), suggesting that ZBP1 is required for robust Z-DNA accumulation in cells experiencing mtDNA stress.

We next sought to determine whether Z-DNA is intrinsically more immunostimulatory to the cGAS-IFN-I axis. Transient transfection of Z-DNA or B-DNA into WT cells elicited comparable ISG expression at early timepoints. However, Z-DNA was significantly more stimulatory at 12–24 hours post transfection (Figure 2I). Z-DNA and B-DNA elicited similar levels of ISGs in $Zbp1^{-/-}$ cells, suggesting that the Z-DNA stabilizing and/or signaling functions of ZBP1 are necessary to augment IFN-I signaling. Additional studies in ARPE-19 cells confirmed findings in MEFs, revealing that Z-DNA is more stimulatory than B-DNA in human cells (Figure S2J). Finally, using an in vitro cGAS activity assay[62], we observed no differences in cGAMP production in the presence of either DNA conformation, indicating that cGAS enzymatic activity is comparably induced by both B- and Z-DNA (Figure S2K). Collectively, these data show that Z-DNA is a potent IFN-I inducer and reveal that torsional mtDNA stress promotes the formation of Z-DNA that is stabilized by ZBP1.

ZBP1 and cGAS form a DNA- and RHIM-dependent complex in the cytoplasm

Although Z-DNA did not stimulate more cGAMP production in vitro, we observed increased cGAMP levels in $Tfam^{+/-}$ and Doxo-exposed cells, which were dependent on ZBP1 (Figures S3A and S3B). We reasoned that increased cGAS activity downstream of mtDNA stress could result from ZBP1-dependent stabilization of Z-DNA ligands for detection by cGAS and/or the redistribution of cGAS to the cytosol. cGAS is predominately a nuclear protein[62,63], yet we observed a significant increase in the proportion of cytosolic cGAS in ARPE-19 cells after TFAM knockdown (Figures S3C and S3D) that was dependent on ZBP1 (Figures S3C and S3D). Doxo treatment also resulted in elevated cGAS expression in cytosolic fractions (Figures S3E and S3F). To next explore whether ZBP1 could impact the distribution of cGAS independently of mtDNA stress, we transfected plasmids encoding human or mouse cGAS and ZBP1 into COS-7 cells. Consistent with the endogenous expression pattern in most cells[63], both human and mouse cGAS localized primarily to the nucleus upon transfection (Figures S3G and 3A). In contrast, cells co-expressing cGAS and full length ZBP1 (ZBP1FL) exhibited higher cytosolic intensity of cGAS, which co-localized with ZBP1 (Figures 3A, 3L, S3G and S3H). Consistent with these microscopy data, we observed a robust interaction between cGAS and ZBP1 in cytosolic immunoprecipitates (Figures 3E and S3I). Fractionation experiments revealed that ZBP1 localized to the cytosol in $Tfam^{+/-}$ as well as IFN-I and Doxo treated cells (Figures S3E, 3B, and 3C). Moreover, co-immunoprecipitation (co-IP) assays in $Tfam^{+/-}$ and Doxo-treated cells demonstrated strong interactions between cGAS and ZBP1 in cytosolic, but not nuclear, extracts (Figure 3B and 3C).

Additional co-IP experiments to identify the domains of cGAS mediating binding to ZBP1 revealed that ZBP1 interacted with both the N-terminal 147 a.a. of cGAS (cGAS N-term), as well as a construct lacking the first 147 amino acids (N-term) (Figure S3J), suggesting that at least two interaction sites bridge cGAS and ZBP1. To define the domains of ZBP1 necessary for interaction with cGAS, we first generated ZBP1 constructs lacking the first

(ΔZα1) or both Z-nucleic acid binding domains (ΔZα1Zα2) (Figure 3D). Upon transient expression of ZBP1 and cGAS constructs, we noted that the ZBP1 ΔZα1Zα2 mutant was attenuated in binding cytosolic cGAS compared to ZBP1FL (Figure 3E, lanes 1 and 3). Using benzonase to degrade cytosolic nucleic acids before co-IP (Figure S3K and S3L), we observed that ZBP1 was less efficient at pulling down cGAS after treatment (Figure S3M), mirroring the weaker interactions observed between the ZBP1 ΔZα1Zα2 mutant and cGAS (Figure 2E). As cGAS and ZBP1 have been reported to bind various endogenous and exogenous nucleic acids[64–68], we next sought to determine if ZBP1-cGAS complexes forming in response to mtDNA instability require DNA or RNA. DNase I or RNase A treatment was sufficient to degrade mtDNA or mtRNA in *Tfam*^{+/−} cells, respectively (Figure 3F). However, only DNase I treatment diminished ZBP1-cGAS binding in *Tfam*^{+/−} cells displaying mtDNA instability (Figure 3G). Finally, we developed a cell-free, in vitro binding assay to examine whether ZBP1 and cGAS interact directly and explore whether the interaction is potentiated by DNA. After expressing full-length mouse cGAS and ZBP1 in *E. coli* and purification by gel filtration chromatography (Figure 3H), we performed in vitro IPs with or without Z- or B-DNA (Figure 3I). Strikingly, these experiments revealed that ZBP1 and cGAS bind directly and that the ZBP1-cGAS complex is stabilized by DNA. Despite increased ZBP1-cGAS interactions in the presence of DNA, ZBP1 did not augment the enzymatic activity of cGAS (Figure S3N). Overall, these data demonstrate that Z-DNA binding domains of ZBP1 nucleate DNA-dependent interactions with cGAS.

As our in vitro IP experiments revealed that ZBP1 and cGAS can bind directly in the absence of DNA, we reasoned that other domains of ZBP1 might contribute to binding. In agreement, we noted that ZBP1 constructs possessing mutated RHIM domains (mRA, mRB) (Figure 3E, lanes 4–5), lacking RHIM A or RHIM B (ΔRA, ΔRB) (Figure S3O), or lacking a 97 a.a. C-terminal region containing the third RHIM domain (ΔC) (Figure 3E, lane 6) weakly interacted with cGAS upon transient expression in 293FT cells. Moreover, a ZBP1 construct of roughly 100 amino acids containing only the RA and RB domains (RA+RB) was able to bind cGAS (Figure 3J). Cells expressing cGAS and ZBP1RA+RB exhibited increased cytosolic cGAS and protein co-localization like those expressing ZBP1FL (Figures 3K and 3L). However, cGAS staining was significantly more nuclear when co-expressed with the ZBP1 ΔRA mutant (Figures 3L and 3M), further supporting the notion that the cGAS and ZBP1 complex forms in the cytosol and is mediated, at least in part, by the ZBP1 RHIM domains.

RIPK1 and RIPK3 localize to the ZBP1-cGAS complex and sustain IFN-I signaling to mitochondrial genome instability

We next sought to clarify the mechanisms by which ZBP1 amplifies IFN-I signaling downstream of mitochondrial genome instability and Z-DNA liberation. Similar to our previous transfection results (Figure 2I), we noted that expression of ISGs early after TFAM silencing (72-hours) was similar between WT and *Zbp1*^{−/−} cells (Figure 4A, lanes 4 and 10). We also observed similar levels of TBK1[S172] and STAT1[Y701] phosphorylation between WT and *Zbp1*^{−/−} cells at the 72-hour timepoint, suggesting that initial detection of cytosolic mtDNA by cGAS, activation of STING/TBK1, and the early production of IFNβ are independent of ZBP1. However, *Zbp1*^{−/−} cells displayed markedly reduced IFIT3 and

STAT1 expression 96 hours post TFAM silencing (Figure 4A, lanes 6 and 12), revealing that ZBP1 is required to sustain IFN-I signaling downstream of mtDNA instability. We also observed that ZBP1 is necessary for phosphorylation of STAT1 on serine 727 at late timepoints after TFAM silencing, noting a near ablation of phospho-STAT1^{S727} in $Zbp1^{-/-}$ cells 96 hours after TFAM knockdown.

Our prior data revealed that both RIPK1 and RIPK3 localize to the DNase-sensitive ZBP1-cGAS complex in $Tfam^{+/-}$ cells (Figure 3G), and therefore we reasoned that RIPK recruitment/activation in the ZBP1-cGAS complex might sustain ISG expression. Interestingly, endogenous IP studies using a cGAS antibody showed that RIPK1 and RIPK3 form a complex with cGAS in WT cells and interact with ZBP1 upon its induction in $Tfam^{+/-}$ MEFs (Figure 4B, top panel). IPs using a ZBP1 antibody revealed that the small amount of ZBP1 in resting WT cells can also form a complex with RIPK1 and RIPK3 that minimally includes cGAS; however, we noted that the ZBP1-cGAS-RIPK1-RIPK3 complex was significantly enriched in $Tfam^{+/-}$ MEFs (Figure 4B, middle panel). Moreover, we observed that knockdown of RIPK1 in $Tfam^{+/-}$ cells was sufficient to reduce total ZBP1 levels and therefore the amount of ZBP1 immunoprecipitating with cGAS, whereas silencing of RIPK3 had no effect on total ZBP1 or abundance of the ZBP1-cGAS complex (Figure 4C, lanes 2 and 3). cGAS also robustly immunoprecipitated both RIPK1 and RIPK3 in $Tfam^{+/-}Zbp1^{-/-}$ MEFs (Figure 4C, lane 4). Finally, transfection of Z-DNA resulted in ZBP1 recruitment to the cGAS complex and augmented the level of RIPK1 co-immunoprecipitating with both proteins (Figure S4A). Collectively, these data suggest a model in which RIPK1 and RIPK3 form basal complexes with both DNA sensors, followed by the assembly of larger ZBP1-cGAS-RIPK1-RIPK3 complexes in the presence of Z-DNA ligands.

Phosphorylation of serine 727 in the transactivation domain of STAT1 is required to fully activate its transcriptional activity and is induced by multiple kinases including p38 MAPK, CDK8, and RIPK1[69–72]. Consistent with a role for RIPK1, we found that RIPK1 silencing dramatically reduced p-STAT1^{S727} levels and ISG expression in $Tfam^{+/-}$ fibroblasts, whereas RIPK3 silencing had more modest effects (Figures 4D and 4E). RIPK1 and RIPK3 inhibitor studies using Necrostatin-1 (Nec-1) and GSK'872 substantiated siRNA studies and revealed that the kinase activities of RIPK1, and RIPK3 to a lesser extent, governed p-STAT1^{S727} levels and sustained ISG expression in MEFs exhibiting mtDNA instability (Figures 4F and 4G). Additional experiments confirmed that ZBP1 and RIPK1 kinase activity were essential for STAT1^{S727} phosphorylation and ISG expression in human cells after TFAM silencing, whereas RIPK3 kinase activity was not as crucial (Figures 4H and 4I). RIPK1 and RIPK3 kinase activities were also required to sustain p-STAT1^{S727} levels and ISG expression after silencing of TOP3A (Figures 4J and S4B) or TOP1MT (Figure S4C), as well as following exposure to Doxo (Figures 4K and 4L). Moreover, we observed that Z-DNA more potently induced IFIT3 in WT cells, likely due to increased STAT1 phosphorylation at serine 727. However, consistent with our ISG expression data (Figure 2I), both Z- and B-DNA induced comparable p-STAT1^{S727} and similar ISG expression in $Zbp1^{-/-}$cells (Figure S4D). Importantly, the kinase activities of RIPK1 and RIPK3 are not required for IFN-I responses triggered by canonical cGAS-STING signaling (Figure S4E), RLR-MAVS signaling (Figure S4F), or cGAS-STING signaling induced by IMM herniation

and release of B-form mtDNA (Figure S4G). Taken together, these data show that following induction of mitochondrial genome stress and Z-DNA liberation, the ZBP1-cGAS complex promotes activation of RIPK1 and RIPK3, which augment STAT1^{S727} phosphorylation, increase expression and transcriptional activity of the interferon-stimulated gene factor 3 (ISGF3) complex, and sustain ISG expression.

ZBP1 is a well-appreciated driver of RIPK3 and mixed lineage kinase domain-like pseudokinase (MLKL)-dependent necroptosis, an inflammatory form of cell death that can be induced by interferon and can feed forward to potentiate IFN-I and pro-inflammatory responses[15,73–77]. To examine the possibility that MLKL promotes mtDNA instability and release in *Tfam*$^{+/-}$ cells, we silenced MLKL by siRNA. Notably, *Tfam*$^{+/-}$ MEFs depleted of MLKL continued to show mitochondrial nucleoid aggregation and elevated ISG expression (Figures S4H–S4J). Moreover, WT and *Tfam*$^{+/-}$ MEFs were similarly susceptible to necroptosis triggered by TNFα+zVAD+CHX treatment (Figure S4K). Cell death triggered by Doxo was also equivalent between WT and *Zbp1*$^{-/-}$ MEFs (Figure S4L). In sum, these results suggest that the ZBP1-cGAS complex senses mtDNA genome instability and engages RIPK1 and RIPK3 to sustain IFN-I signaling independently of MLKL and a feed forward loop of cell death.

Doxorubicin induces a ZBP1-dependent IFN-I response in cardiomyocytes

Top1mt$^{-/-}$ mice exhibit increased mtDNA instability, mitochondrial dysfunction, and cardiac injury after Doxo[34]. Consistent with our findings in fibroblasts, we also noted increased ISG expression in neonatal cardiomyocytes (CMs) after TOP1MT knockdown, which was entirely dependent on ZBP1 (Figure S5A). Early work in rodents reported the preferential accumulation of cardiac mtDNA damage after Doxo that lingered for weeks after administration[33]. Given the high mtDNA content in CMs, we hypothesized that Doxo might trigger mtDNA genome instability and cytosolic release in CMs, leading to elevated ZBP1-cGAS signaling and IFN-I responses. We first mined two publicly available microarray datasets of CMs challenged with Doxo[78,79]. Gene set enrichment analysis showed that Doxo treatment increased expression of innate immune and inflammatory genes, including those associated with IFN-I, TNFα, and DNA damage signaling (Figures 5A and S5B). Furthermore, analysis of differentially expressed genes across all datasets indicated that IFN-I signaling (Interferon Alpha Response) was the most heavily enriched network (Figure 5A). In line with these bioinformatic analyses, Doxo strongly upregulated type I interferons, ZBP1, and other ISGs in human induced pluripotent stem cell-derived CMs (hiPSC-CMs) and murine neonatal CMs in a time dependent fashion (Figures 5B and 5C). Treatment of CMs with IFNAR blocking antibody further confirmed that IFN-I, but not IFNγ or NF-κB signaling, was responsible for Doxo-induced ISG expression (Figures 5D and 5E). Suggestive of a role for Doxo in promoting mitochondrial stress, exposure of hiPSC-CMs to Doxo caused pronounced mtDNA nucleoid aggregation, mitochondrial network hyperfusion, and the accumulation of cytosolic DNA (Figure 5F). Moreover, Doxo treatment increased the intensity of Z-DNA in CMs, which was significantly reduced in cells depleted of ZBP1 (Figures 5G, 5H, and S5C). ZBP1 silencing also attenuated expression of Doxo-induced ISGs in hiPSC-CMs (Figure 5I), and Doxo failed to induce robust ISG expression in *Ifnar*$^{-/-}$, *Sting*$^{-/-}$, and *Zbp1*$^{-/-}$ neonatal CMs (Figure 5J). Collectively, these

results indicate that Doxo promotes mtDNA genome instability in CMs, leading to Z-DNA accumulation that triggers the ZBP1-cGAS-IFN-I signaling axis.

Clinical case reports have linked IFNα immunotherapy to cardiomyopathy and other serious cardiac complications[80–85], yet the direct effects of IFN-I on CM function have not been characterized. Interestingly, we observed that hiPSC-CMs are highly responsive to IFN-I (Figure S5D). Interestingly, IFN-I treatment increased expression of markers of CM injury (Figure S5E), while reducing expression of mtDNA-encoded OXPHOS genes (Figure S5F). Reduced mtDNA-encoded OXPHOS gene expression was also observed in murine neonatal CMs exposed to IFNβ or Doxo (Figure S5G). Using a real-time imaging assay to measure hiPSC-CM beat rate and morphological appearance, we observed that both IFN-I and Doxo treatment altered CM beat periodicity and induced significant vacuolization after prolonged exposure (Figure S5H). Together, these results indicate that Doxo-induced mtDNA instability triggers a ZBP1-dependent IFN-I response that potentiates CM dysfunction.

Doxorubicin induces IFN-I responses in cardiomyocytes and cardiac myeloid cells in vivo

To next determine the cellular sources and immediate kinetics of cardiac IFN-I after in vivo Doxo challenge, we employed a high dose, acute exposure protocol and assessed gene expression in CMs by RNA-seq and IFN-I activation in non-CM populations by flow cytometry (Figure 6A). Expression profiling of highly enriched CMs extracted from Doxo-exposed hearts[86,87] uncovered a striking upregulation of innate immune signatures mirroring our in vitro studies. Pathway analysis revealed 'Interferon Alpha Response' as the most significantly up-regulated node in CMs post-Doxo challenge (Figure 6B), with *Zbp1* representing the most highly expressed ISG (Figure 6C and Table S2). Analysis of the top downregulated pathways revealed strong inhibition of metabolic and myogenesis-related genes, with 'Oxidative Phosphorylation' representing the most inhibited node in CMs from Doxo-challenged hearts (Figure 6D). Numerous genes functioning in mitochondrial oxidative metabolism were downregulated in CMs (Figure 6E and Table S2), which is consistent with the well-appreciated mitochondrial toxicity of Doxo. Western blotting of purified CMs confirmed our RNA-seq results and showed elevated ZBP1 and IFIT3 along with reduced OXPHOS subunits ATP5A1, SDHB, and NDUFB8 from Doxo-exposed hearts relative to vehicle controls (Figure S6A). Utilizing a tamoxifen inducible, CM-specific Cre recombinase expressing strain (*αMHC-MerCreMer*) crossed onto *Sting^fl/fl* and *Ifnar^fl/fl* mice (Figures S6B), we observed that ablation of the cGAS-STING pathway or IFN-I signaling reduced ZBP1 expression in cardiac lysates, and other ISGs to a lesser extent (Figure S6C). This indicates that CMs in vivo are capable of directly sensing Doxo-induced DNA damage via STING and responding to IFN-I, but also reveals that other cardiac cell types contribute to IFN-I responses in the Doxo-exposed heart.

To complement our enriched CM RNA-seq data and identify non-myocyte populations contributing to IFN-I responses in the heart after Doxo challenge, we utilized a *Mx1^gfp* ISRE reporter mouse that expresses GFP under control of the IFN-I-regulated, endogenous *Mx1* locus[88]. We focused on abundant non-CM populations including Ter119⁻CD45⁺ immune cells, Ter119⁻CD45⁻CD31⁺ endothelial cells, and Ter119⁻CD45⁻CD31⁻CD90.2⁺

fibroblasts[89]. Using these multiplex panels, we observed that Doxo promoted remodeling in all non-myocyte cardiac cell populations, with a notable decrease in endothelial cells and an increase in fibroblasts (Figure 6F). Although $CD45^+CD11b^-$ cardiac lymphoid populations decreased after Doxo, the percentage of $CD45^+CD11b^+$ myeloid immune cells remained constant (Figures 6G). However, $CD45^+CD11b^+$ cells expressing platelet/endothelial cell adhesion molecule 1 (PECAM-1; CD31), which governs leukocyte transmigration through vascular endothelial cells and recruitment into inflamed tissues, were increased in Doxo-exposed hearts (Figure 6H)[90,91]. Despite significant changes in cardiac $CD45^-$ cell numbers and $CD45^+CD11b^-$ lymphocyte abundance, $Mx1^{gfp}$ intensity was not altered in either population after Doxo treatment (Figures S6D and S6E). However, $Mx1^{gfp}$ expression was markedly increased in $CD45^+CD11b^+$ cardiac myeloid cells (Figures 6I and 6J) comprised of $Ly6C^+$ monocytes (Figure 6K) and $Ly6C^-$ macrophages and dendritic cells (Figure 6L)[92]. Most $Ly6C^+$ monocytes exhibiting high $Mx1^{gfp}$ also expressed CD31 in Doxo-exposed hearts relative to vehicle controls (Figure 6M). In contrast, $CD11b^+CD31^-$ cells did not exhibit significant increases in $Mx1^{gfp}$ (Figure 6N), indicating that recruited myeloid cells are largely responsible for non-CM IFN-I signaling post-Doxo. Consistent with a role for myeloid immune cells in the cardiac IFN-I program induced by Doxo, conditional ablation of STING (*Sting$^{fl/fl}$LysMcre*) or IFNAR (*Ifnar$^{fl/fl}$LysMc*re) in myeloid cells (Figure 6O) markedly reduced ZBP1 and other ISGs in cardiac lysates (Figure 6P). Finally, we observed that ZBP1 is upregulated in cardiac extracts and interacts strongly with cGAS after in vivo Doxo challenge (Figure S6F). Collectively, these data suggest that Doxo induces significant cardiac remodeling, robust ZBP1-cGAS complex assembly, and IFN-I responses in vivo.

Adjuvant IFNα synergizes with Doxorubicin to enhance cardiac and mitochondrial dysfunction in tumor-bearing mice

In order to advance mechanistic understanding of IFN-I-mediated cardiotoxicity, we merged an autochthonous melanoma model[93,94] with an extended Doxo protocol that more closely resembles clinical timelines in late DIC (Figure S6G). Doxo chemotherapy significantly restricted melanoma growth, with adjuvant IFNα providing a modest synergistic effect (Figure S6H). Transthoracic echocardiographic analyses four weeks after cessation of Doxo chemotherapy revealed reduced left ventricular ejection fraction (EF), fractional shortening (FS) and left ventricle (LV) mass in tumor-bearing mice (Figure S6I). This was accompanied by significant LV dilation, wall thinning, and cardiac fibrosis (Figures S6J–S6L). Consistent with our acute Doxo challenge model, we noted that ZBP1 and other ISGs were elevated in Doxo-exposed hearts relative to mice receiving vehicle only (Figure S6M). Strikingly, adjuvant IFNα treatment further exacerbated LV dysfunction, fibrosis, and cardiac ISG expression compared to the Doxo only group (Figures S6I–S6M). Finally, melanoma bearing mice receiving Doxo and IFNα showed reduced OXPHOS protein expression and cardiac mtDNA abundance (Figures S6N and S6O). These results suggest that IFN-I signaling synergizes with Doxo to promote loss of mtDNA and OXPHOS subunit expression, which correlate with increased cardiac fibrosis and heart failure.

ZBP1 regulates cardiac IFN-I responses that contribute to Doxorubicin-induced cardiomyopathy

As our data indicate that multiple cardiac populations contribute to IFN-I responses that potentiate Doxo-induced cardiac dysfunction, we next employed a chronic Doxo dosing regimen on ZBP1, STING, and IFNAR constitutive knockouts (Figure 7A). Echocardiography of WT mice revealed marked impairments in cardiac functional measures after Doxo (Figure 7B). In contrast, mice lacking ZBP1, STING or IFNAR exhibited higher EF and FS compared to WT throughout the longitudinal study (Figure 7B). In depth analysis of longitudinal echocardiographic measurements showed that $Zbp1^{-/-}$, $Sting^{-/-}$ and $Ifnar^{-/-}$ mice displayed less Doxo-induced wall thinning, LV dilation, and weight loss compared to WT controls (Figures 7C, 7D and S7A–S7C). To link cardiac dysfunction with sustained IFN-I signaling, we examined transcript and protein abundance of ISGs seven weeks after the cessation of Doxo injection. WT mice exhibited sustained expression of ISGs assayed at week 10 post-Doxo. In contrast, ZBP1 and other ISGs were significantly lower or not induced in Doxo-exposed $Zbp1^{-/-}$, $Sting^{-/-}$ and $Ifnar^{-/-}$ mice (Figures 7E and S7D). Moreover, all knockout strains exhibited reduced cardiac expression of gene signatures associated with heart failure (Figure 7F). Histologic analyses of Doxo-challenged $Zbp1^{-/-}$, $Sting^{-/-}$ and $Ifnar^{-/-}$ mice revealed less CM vacuolization (Figures 7G and S7E) and reduced cardiac fibrosis (Figures 7H and S7F) at week 10 compared to WT controls. Finally, Doxo-induced OXPHOS subunit loss as measured by ATP5A1 immunofluorescence staining was significantly lessened in $Zbp1^{-/-}$, $Sting^{-/-}$ and $Ifnar^{-/-}$ mice (Figures 7I and S5G). Additional analysis of $Sting^{-/-}$ and $Ifnar^{-/-}$ cardiac lysates revealed higher levels of mtDNA and OXPHOS subunit expression after Doxo relative to WT controls (Figures S7H and S7I). In summary, our data reveal that the ZBP1-cGAS-STING axis governs cardiotoxic IFN-I signaling, which contributes significantly to the pathobiology of chemotherapy-related heart failure.

DISCUSSION

ZBP1 has emerged as a central innate immune sensor of double-stranded nucleic acids in the left-handed, Z-conformation[14–22,64], and our study adds Z-form mtDNA to the growing list of ZBP1 ligands. Moreover, our work reveals that both genetic and pharmacologic triggers of mitochondrial genome instability can induce Z-form mtDNA in cellulo. Our data show that increased negative mtDNA supercoiling in cells lacking TFAM, TOP3A, and TOP1MT favors B to Z transition, leading to the accumulation of mitochondrial Z-DNA for detection by ZBP1. In contrast, we noted that ZBP1 is not required for sensing cytosolic B-form mtDNA liberated by IMM herniation. Therefore, the cytosolic DNA sensing machinery can discriminate between different mtDNA species, with the ZBP1-cGAS complex functioning as a specialized PRR for Z-form mtDNA.

Since overall Z-DNA intensity is lower in $Zbp1^{-/-}$ cells, it is likely that the Zα domains of ZBP1 stabilize Z-DNA and sustain detection by cGAS to augment IFN-I signaling. Moreover, the RHIM domains of ZBP1 are required for maximal cytosolic interactions with cGAS. ZBP1 forms homotypic interactions with the RHIM domain-containing proteins RIPK1 and RIPK3 to mediate NF-κB activation and innate immune signaling, as well

as promote RIPK3-MLKL-dependent necroptosis[15,95–98]. However, MLKL-mediated cell death does not impact IFN-I responses in cells experiencing mitochondrial genome instability. Consistent with immune signaling roles for RIPK1 and RIPK3, we found that both kinases are present in the ZBP1-cGAS complex. Moreover, the kinase activities of RIPK1 and promote STAT1^{S727} phosphorylation in response to mitochondrial Z-DNA accumulation and are required to sustain the ZBP1-dependent IFN-I program. These findings are in line with a recent study showing that ZBP1 interacts with cGAS, RIPK1, and RIPK3 in *Casp8*$^{−/−}$/*Mlkl*$^{−/−}$ MEFs and sustains STAT1 phosphorylation to Z-RNA[99]. Future studies should determine whether CASP8, FADD, and/or MLKL activities are inhibited in cells experiencing mitochondrial genome instability, which might favor ZBP1-cGAS-RIPK signaling to STAT1 while repressing ZBP1-dependent cell death signaling.

Doxo and other anthracycline chemotherapeutics are among the most effective and widely used antineoplastic drugs, however their clinical application is limited by adverse cardiac side effects that occur in many patients[100]. Importantly, we have uncovered that Doxo induces mtDNA instability and Z-DNA accumulation in CMs and triggers a robust cardiac IFN-I signature that is dependent on ZBP1, STING, and IFNAR. Our data also reveal that CMs and infiltrating myeloid cells respond to Doxo by activating ZBP1-dependent IFN-I responses. Using a Doxo dosing protocol that closely resembles clinical timelines in late DIC, we observed that ZBP1 and other ISGs remain elevated in the heart for weeks after the last Doxo dose, suggestive of a self-propagating IFN-I cycle. Although cGAS and IFN-I signaling have recently been implicated in heart failure[38,41,101–103], a role for ZBP1 has not been explored. Our findings indicate the presence of a ZBP1-dependent IFN-I signaling program in cardiac cells exposed to Doxo and highlight that ZBP1 is a key innate immune regulator of DIC and cardiomyopathy. Therefore, ZBP1 is a promising therapeutic target in chemotherapy-related cardiac dysfunction and perhaps other cardiovascular diseases where mtDNA instability promotes detrimental IFN-I and inflammatory responses.

LIMITATIONS OF THE STUDY

Although we observed increased Z-DNA staining in mitochondria and the cytoplasm after induction of mitochondrial genome instability, we did not identify the precise Z-DNA sequences that are stabilized by ZBP1. Mitochondrial dysfunction and mtDNA replication defects can feed forward to cause nuclear genome instability[104,105], and therefore it is possible that Z-DNA derived from both mtDNA and nuclear DNA accumulate in our models. Second, although we find that mitochondrial genome instability upregulates ZBP1 and promotes ZBP1-cGAS interactions, both DNA sensors form basal complexes with RIPK1 and RIPK3. Our study does not elucidate the stoichiometry of these complexes, nor identify the molecular changes that license RIPK-dependent phosphorylation of STAT1 as opposed to MLKL. Finally, although mtDNA instability predominantly drives ZBP1-cGAS-RIPK-dependent IFN-I signaling in vitro, we cannot exclude a role for ZBP1-driven cell death in DIC in vivo.

STAR METHODS

RESOURCE AVAILABILITY

Lead contact—Further information and requests for resources and reagents should be directed to and will be fulfilled by the lead contact, A. Phillip West (awest@tamu.edu).

Materials availability—All primary cells, plasmids, and mouse strains generated in this study are available from the Lead Contact with a completed Materials Transfer Agreement.

Data and code availability—All data needed to evaluate the conclusions drawn herein are present in the paper and/or the supplementary figures and tables. Any additional information required to reanalyze the data reported in this paper is available from the lead contact upon request. RNA-seq datasets have been deposited in the Gene Expression Omnibus under accession numbers GSE223553 and GSE223698. Additional confirmatory data from Figures 1G, 1H, 2D, 2H, 2I, 3A, S3C, and 5H were deposited on Mendeley at doi: 10.17632/cnw3htbbm9.2.

EXPERIMENTAL MODEL AND SUBJECT DETAILS

Mouse husbandry and strains—C57BL/6J (strain 000664), *LysMCre* (strain 004781), *αMHC-MerCreMer* (strain 005657), *Sting$^{fl/fl}$* (strain 031670), *Ifnar1$^{fl/fl}$* (strain 028256), *Mx1^{gfp}* (strain 033219), *Sting$^{-/-}$* (*Sting1^{gt}*; strain 017537) and *Ifnar1$^{-/-}$* (MMRRC Strain #032045-JAX) mice were purchased from The Jackson Laboratory. *Mavs$^{-/-}$* (strain 008634) mice were purchased from The Jackson Laboratory and were backcrossed onto the C57BL/6J background for 10 generations before use. *Tfam$^{+/-}$* mice were previously reported[36,42]. *Zbp1$^{-/-}$* mice[48] were obtained collaboratively from Dr. Ken Ishii and were backcrossed onto the C57BL/6J background for at least 4 generations before use. Breeding colonies of all strains were established and maintained on the C57BL/6J background at Texas A&M University. Mice were group-housed in humidity-controlled environments maintained at 22°C on 12-hour light–dark cycles (600–1800). Food and water were available ad libitum. All animal procedures were approved by the Texas A&M Animal Care and Use Committee (TAMU IACUC). The euthanasia methods employed in the study are consistent with the recommendations of the American Veterinary Medical Association (AVMA).

Doxorubicin administration—Male and female mice between 8–12 weeks of age were housed in a standard 12-h light/dark cycle with unlimited access to food and water. Doxorubicin stock solution (10 mg/mL) was prepared in cell culture grade water (VWR, 82007–330) and used within 28 days. Further dilutions were made in DPBS (Sigma-Aldrich, D8537) on the day of injection. In Figure 6, *Mx1^{gfp}*, WT*LysMcre*, *Sting$^{fl/fl}$LysMcre* and *Ifnar$^{fl/fl}$LysMcre* mice were intraperitoneally (i.p.) injected with one dose of 25 mg/kg of Doxorubicin. In Figure S6, Cre expression was induced by 3 i.p. injections of 30 μg/g of tamoxifen into WT *αMHC-MerCreMer*, *Sting$^{fl/fl}$ αMHC-MerCreMer* and *Ifnar$^{fl/fl}$ αMHC-MerCreMer* mice, followed by 4-weeks or rest, and of one i.p. injection of 25 mg/kg of Doxorubicin. In Figure 7, i.p. injection of Doxorubicin (5 mg/kg body weight, 100 μL injection volume) was performed weekly for four continuous weeks (cumulative dose 20 mg/kg body weight).

Mouse melanoma induction, Doxorubicin and adjuvant IFNα therapy—An autochthonous model of melanoma was utilized in Figures S6G–S6O, and melanomas were induced on equal numbers of 21-day-old male and female mice as described in Dankort et al. 2009[93]. First, mice were anesthetized by isoflurane, then a commercial topical depilatory cream was applied to remove hair from roughly 2 cm^2 on the lower dorsal region of mice approximately 1–2 cm from the base of the tail. The next day, mice were anesthetized with isoflurane and 1 μL of a 20 mM solution of 4-hydroxytamoxifen (Hello Bio, HB6040) dissolved in ethanol was applied topically to the exposed skin. Four weeks after melanoma induction, hair was removed from the lower dorsal region of the mice using hair trimmers to allow confirmation of tumor induction and monitoring of tumor growth. Tumors were measured for width, length, and height every 2–4 days using digital calipers in order to calculate tumor volume. Mice received vehicle (PBS) or Doxorubicin (5 mg/kg body weight, 100 μL i.p. injection volume) weekly for four consecutive weeks (cumulative dose 20 mg/kg body weight). Adjuvant IFNα (20,000 units) was co-administrated together with Doxorubicin in a total volume of 100 μL or diluted with PBS in a total volume of 50 μL and i.p. injected alone as indicated in Figure S6H.

Cardiac cell isolation—Cardiac cell isolation was performed as described by Ackers-Johnson et al.[86] with some modifications. Briefly, 8–12-week-old, male and female *Mx1^{gfp}* mice i.p. injected with saline or Doxorubicin were anaesthetized using an isoflurane vaporizer, and anesthesia was maintained using a nose cone throughout the surgical procedure. Following anesthesia, thoracic cavities were opened to expose the heart. The descending aorta was severed to allow exsanguination, and 7 mL EDTA buffer was immediately injected into the right ventricle. Next, the ascending aorta was clamped using a hemostat, and the heart was removed then transferred to a 60 mm dish containing fresh EDTA buffer, then again injected with 10 mL EDTA buffer into the left ventricle at 2 to 3 mm above the heart apex. Next, the heart was transferred to a 60 mm dish containing perfusion buffer and injected with 3 mL of perfusion buffer through the same perforation on the left ventricle. Then, the heart was transferred to a 60 mm dish containing collagenase buffer, and digestion was achieved by continuously injecting collagenase buffer through the same perforation at the flow rate approximately 2 mL/min until the heart turned pale and flaccid and the injection perforation was enlarged. The atria and ventricles were gently separated, and then the ventricles (with septum) were transferred to a new 60 mm dish containing 3 mL fresh collagenase buffer. The digested tissues were pulled into 1 mm pieces using fine-tip forceps, single cardiac cells were dissociated by gently trituration, and finally the enzyme activity was neutralized by adding 5 mL stop buffer. Cell suspension was filtered through a 70 μm strainer, and cardiomyocytes were settled by gravity for 20 min in a 50 mL tube. The supernatant containing non-myocyte cardiac cells was subjected to staining for flow cytometry analysis, and the cardiomyocyte pellet was preserved for RNA and protein extraction for further analysis. All buffers were prepared in cell-culture grade water and recipes can be found in Ackers-Johnson et al[86], with the exception that 2,3-butanedione monoxime (BDM) was replaced with 5mM blebbistatin (Selleckchem, S7099). EDTA, perfusion, and collagenase buffers were apportioned into 10 mL syringes with 27 G needles and 60 mm dishes, then kept warm at 37 °C.

Cell culture—Primary WT, *Tfam*^{+/−}, *Zbp1*^{−/−}, and *Tfam*^{+/−}*Zbp1*^{−/−} MEFs were generated from E13.5–14.5 male and female embryos, maintained in DMEM (Sigma-Aldrich, D5796) supplemented with 10% low endotoxin FBS (VWR, 97068–085), and sub-cultured no more than five passages before experiments. Murine neonatal cardiomyocytes were isolated from 2–3-day-old male and female neonates with the Neonatal Cardiomyocyte Isolation Kit (Miltenyi Biotec, 130–098-373). Human iPSC-derived cardiomyocytes were purchased from Fujifilm Cellular Dynamics (01434) and cultured as described in the manual. 293FT cells were purchased from Invitrogen (R70007). COS-7 (CRL-1651) and ARPE-19 (CRL-2302) cells were purchased from ATCC.

METHOD DETAILS

siRNA and DNA transfection—siRNA transfection was performed with 25 nM siRNA duplexes and 3 μL of Lipofectamine RNAiMAX reagent (ThermoFisher Scientific, 13778150) according to the manufacturer's protocol. DNA transfection was performed with polyethylenimine, PEI (Alfa Aesar, 43896) at a ratio of 5:1 PEI to nucleic acids.

Southwestern Blot—mtDNA isolation and southwestern blotting were performed as described previously[47]. In brief, MEFs were treated with 10 μM aphidicolin (Hello Bio, HB3690) for 4 h, after which 50 μM BrDU (Invitrogen, B23151) was added to the culture medium for an additional 24 h. Following treatment, DNA was isolated using the E.Z.N.A.® plasmid DNA minikit (Omega bio-tek, D6942–02), and 1 μg of isolated DNA was loaded and run on a 0.45% agarose gel in TBE (26 V at 4 °C for 18–20 h). After electrophoresis, the agarose gel was washed with water and soaked in denaturing buffer (0.5M NaOH, 1.5M NaCl) for an hour with gentle shaking. Afterwards, the gel was rinsed again with water and soaked in 10X SSC for 30–60 min before capillary transfer to an ImmobilonP membrane (Millipore Sigma), as described previously[106]. Once transferred, the membrane was soaked in 6X SSC before undergoing UV cross-linking (UV Stratalinker 1800). The cross-linked membrane was blocked with 10% milk in TBST for 1 h, followed by immunoblotting with anti-BrdU antibody (BD Biosciences, 555627) for 2 h at room temperature. The membrane was then washed and incubated with HRP-linked anti-mouse IgG (EMD Millipore Etobicoke) for 1 h, after which the blot was developed using Supersignal West Femto enhanced chemiluminescence substrate (ThermoFisher Scientific) and imaged with a chemiluminescence imaging analyzer (Fujifilm, LAS3000mini).

Cloning and retroviral transduction—Murine STING-HA (InvivoGen) was subcloned into the pMXs-IRES-Puro vector and replication incompetent retroviruses were packaged using Platinum-A cells (Cell Biolabs, RV-102) according to the manufacturer's instructions. 293FT were exposed to supernatants containing pMXs-IRES-Blast-STING-His retroviruses and 4 μg/mL polybrene (Millipore, TR-1003-G). Two days post transduction, 10 μg/mL blasticidin was added to select a stable expression population.

Topologically constrained Z-DNA synthesis—Circular Z-DNA and B-DNA were synthesized as described by Zhang et al.[53]. Briefly, 74-mer oligos containing a 5' phosphate modification (Sigma-Aldrich) were ligated to form circular single-stranded DNA (ssDNA) using a stepwise reaction. The 150 μL reaction mixture contained 25 μM splint, 75 U

T4 ligase (ThermoFisher Scientific, EL0011), and 0.1X T4 ligase buffer. A second mix contained the corresponding 74-mer DNA oligo at 22 μM in 150 μL 0.1X T4 ligase buffer. 15 μL of the DNA mix was added to the reaction mix every 20 min for a total of 10 additions bringing the total reaction volume to 300 μL. After the final addition of DNA, the reaction was allowed to continue for another 12 h. The reaction was carried out at 20 °C and terminated by incubation at 65 °C for 10 min. Any remaining linear DNA was degraded by addition of 35 μL 10X Exonuclease I buffer and 20 μL Exonuclease I (ThermoFisher Scientific, 720735KU) and incubation at 37 °C for 2 h followed by 80 °C for 20 min. Circular ssDNA strands were purified by phenol/ chloroform extraction and ethanol precipitation.

ssDNA strands were annealed to form double-stranded B- or Z-DNA as follows. The annealing reaction contained 10 mM HEPES and 10 mM $MgCl_2$ at pH 7.5. Topologically constrained Z-DNA was obtained by annealing circular 74F ssDNA to circular 74R ssDNA strands at a 1:1 molar ratio. DNA strands were annealed in a thermocycler using the following steps: 90 °C for 5 min, cool to 60 °C at 0.1 °C/s, hold at 60 °C for 10 min, cool to 20 °C at 0.1 °C/s, and hold at 12 °C. B-DNA was made by annealing linear 74F ssDNA to circular 74R ssDNA or annealing circular 74F ssDNA to linear 74R ssDNA as described above. After annealing, fully double-stranded B-DNA was obtained by incubating the dsDNA with T4 ligase in 1X T4 ligase buffer for 12 h at 25 °C followed by incubation with Exonuclease I for 2 h at 37 °C and exonuclease inactivation at 80 °C for 20 min. Both B-DNA and Z-DNA were then purified by phenol/ chloroform extraction and ethanol precipitation. Purified DNA pellets were redissolved in 10 mM HEPES buffer (10 mM $MgCl_2$, pH 7.5).

Electrophoretic Mobility Shift Assay (EMSA)—Circular Z- and B-DNA were diluted to 10 ng/μL (0.43 μM) in 10 mM HEPES buffer (10 mM $MgCl_2$, pH 7.5) and incubated with anti-Z-DNA antibody (Absolute antibody, Ab00783–23.0) at a 1:1 or 1:3 DNA:antibody molar ratio for 4 h at 25 °C. DNA-antibody complexes were resolved by electrophoresis on native 10 % TBE-polyacrylamide gels (ThermoFisher Scientific, EC6275BOX). DNA was visualized by post-staining with SYBR Green I (MedChemExpress, HY-K1004) and imaging on a Bio-Rad ChemiDoc MP Imaging System.

Protein expression and purification—Full length mouse ZBP1 and mouse cGAS were cloned into a modified pET28a vector with a N-terminal Avi-His6-Sumo tag. Both ZBP1 and cGAS were expressed in *E. coli* BL21(DE3) with 0.4 mM isopropyl β-D-1-thiogalactopyranoside (IPTG) induction overnight at 15 °C. Proteins were purified using Ni-NTA agarose (QIAGEN), followed by size-exclusion chromatography using HiLoad 16/600 Superdex200 columns (GE Healthcare Life Sciences). The Avi-His6-Sumo tag was cleaved by sumo protease and removed using Superdex200 columns. Mouse ZBP1 was eluted in the buffer containing 20 mM Tris-HCl pH 7.5, 150 mM NaCl. Mouse cGAS was eluted in the buffer containing 20 mM Tris-HCl pH 7.5, 500 mM NaCl.

cGAS activity assay—The cGAS activity assay was performed in 20 mM HEPES pH 7.5, 150 mM NaCl, 5 mM $MgCl_2$, 5 mM DTT, 2.5 mM ATP, 2.5 mM GTP. 2 μM mouse cGAS was incubated with 0.1 μg/μL B-DNA or Z-DNA with or without 2 μM mouse ZBP1

for 1 h at 37 °C. 2 μM mouse cGAS was incubated with 0.1 μg/μL salmon sperm DNA (Invitrogen, 15632–011) or no DNA for 1 h at 37 °C as the positive and negative control. Reactions were quenched by adding 20 mM EDTA. The products were filtered by 10 kDa-cutoff Amicon Ultra centrifugal filters to remove DNA and proteins and then analyzed by a Mono Q 5/50 GL column (GE Healthcare Life Sciences).

Co-immunoprecipitation—For Figures 3B and 3C, MEFs were treated with 10 ng/mL of mouse IFNβ for 6 hrs or in 50 nM of Doxo for 48 hrs, respectively, before co-IP. The cytosolic fraction was obtained by lysing the cells with NP-40 lysis buffer (50 mM Tris pH7.5, 0.15 M NaCl, 1 mM EDTA, 1% NP-40 and 10% Glycerol), and nuclear fraction was acquired using Nuclear Complex co-IP kit (Active Motif, 54001), which allows a gentle release of DNA-bound protein complexes in the nucleus. Rabbit TrueBlot® Set (Rockland, 88–1688-31) was used for both pre-cleaning and co-IP from both fractions. Mouse TrueBlot® Set (Rockland, 88–7788-31) was used for pre-cleaning and co-IP with ZBP1 antibody in Figure 4B. For co-IPs of cGAS and ZBP1 constructs in 293FT (Figures 3E, 3J, S3I, S3J, S3M and S3O), Pierce™ Control Agarose Resin (ThermoFisher Scientific, 26150) and Anti-DYKDDDDK Tag (L5) Affinity Gel Antibody (Biolegend, 651502) were used for pre-cleaning and IP, respectively. Due to different subcellular localizations of cGAS mutants, the cytosolic fraction and nuclear fraction were obtained as described above, combined and then used for co-IPs of cGAS mutants and ZBP1 in 293FT (Figures S3J). For cell-free co-IP in Figure 3I, protein and DNA are mixed at molar ratio of 1:2. To degrade cytosolic nucleic acids in Figure S3M before co-IP, NP-40 cell lysates were incubated with 10 U/μL of benzonase (Millipore, 71205–3) for 4 h at 4 °C. BSA was added to the samples that were not treated with benzonase to even protein concentration. 20 μL of sample was separated and the benzonase was inactivated by adding 0.5 μL of 0.5 M EDTA and heating to 95°C for 15 min. 10 ng/μL DNA was used in qPCR to amplify mtDNA using primers against mt-ND1. To degrade cytosolic DNA or RNA in Figure 3G before co-IP, NP-40 cell lysates were incubated with 100 μg/mL of DNase I (Worthington Biochemical, LS002139) or 50 μg/mL of RNase A (Worthington Biochemical, LS005650) for 4 h at 4 °C. After incubation, DNA was extracted using Phenol/chloroform and 10 ng/μL DNA was used in qPCR to amplify mtDNA using primers against mt-ND2; RNA was extracted using Quick-RNA microprep kit (Zymo Research, R1051) and subjected to qRT-PCR to amplify *16s* RNA.

Subcellular fractionation, DNA isolation and slot blotting—3×10^6 MEFs were seeded in 15 cm dishes overnight and treated with vehicle or 500 nM of Doxo for 24 hrs. Subcellular fractionation and DNA isolation were performed as previously described[107]. In brief, cells were lysed in digitonin lysis buffer (150 mM NaCl, 50 mM HEPES pH 7.4, and 5 μg/mL digitonin), incubated end over end for 10 min at 4 °C, and centrifuged at 950 × g for 5 min at 4 °C. The cytosolic supernatants were transferred into a new tube and saved as cytosolic fraction, and the pellets were lysed in NP-40 lysis buffer (50 mM Tris pH 7.5, 0.15 M NaCl, 1 mM EDTA, 1% NP-40 and 10% Glycerol). After centrifugation of NP-40 lysates at 21130 × g for 10 min at 4 °C, the supernatants were transferred and saved as mitochondrial fraction, and the nuclei pellets were further lysed in and SDS lysis buffer (20 mM Tris pH 8 and 1% SDS). SDS lysates were boiled at 95°C for 5 min and centrifuged at

21130 × g for 5 min at RT. The supernatants were transferred and saved as nuclear fraction. All fractions were treated with 50 μg/mL of RNase A for 1.5 hrs at 37°C and 200 μg/mL of Proteinase K for 1 h at 55°C before being subjected to Phenol-Chloroform based DNA isolation. After DNA isolation, 200 μg of cytosolic DNA, 1 mg of mitochondrial DNA and 50 μg of nuclear DNA were blotted onto 0.45 μm Nylon membranes (Whatman, 10416230). After air drying, membranes were incubated in primary antibodies at 4°C overnight in 1X PBS containing 1% casein, HRP-conjugated secondary antibody at room temperature for 1 h, and then developed with Luminata Crescendo Western HRP Substrate (Millipore, WBLUR0500).

Quantitative PCR—To measure relative gene expression by qRT–PCR in cells and tissues, total cellular RNA was isolated using Quick-RNA microprep kit (Zymo Research, R1051). Approximately 0.5–1 μg RNA was isolated, and cDNA was generated using the qScript cDNA Synthesis Kit (Quanta, 95047–100). cDNA was then subjected to qPCR using PerfeCTa SYBR Green FastMix (Quanta, 84069). Technical triplicates were run each biological sample, and average expression values were normalized against *Rpl37* cDNA using the $2^{-\Delta\Delta CT}$ method[107]. For mtDNA abundance assessment, 10 ng/μL of template DNA was used for qPCR, and expression values of each replicate were normalized against nuclear-encoded *Tert or RNA18S*[107].

Immunoblotting—Cells and tissues were lysed in NP-40 lysis buffer or SDS lysis buffer supplemented with protease inhibitor (Roche, 04693159001) and then centrifuged at 4 °C to obtain cellular lysate. After BCA protein assay (ThermoFisher Scientific, 23235), equal amounts of protein (10–40 μg) were loaded into 10–20% SDS–PAGE gradient gels and transferred onto 0.22 μM PVDF membranes (Bio-Rad, 1620177). After air drying to return to a hydrophobic state, membranes were incubated in primary antibodies at 4 °C overnight in 1X PBS containing 1% casein, HRP-conjugated secondary antibody at room temperature for 1 h, and then developed with Luminata Crescendo Western HRP Substrate (Millipore, WBLUR0500). For cGAS quantifications in Figures S3E and S3F, cytosolic cGAS expression was normalized to GAPDH, and nuclear cGAS was normalized to LMNB1. These normalized values were used to calculate the percentage of cGAS in the cytosolic (cytosolic cGAS/ total cGAS) and nuclear (nuclear cGAS/ total cGAS) compartments.

Immunofluorescence microscopy—Cells were grown on coverslips and treated as described. After washing in PBS, cells were fixed with 4% paraformaldehyde for 20 min, permeabilized with 0.1% Triton X-100 in PBS for 5 min, blocked with PBS containing 5% FBS for 30 min, stained with primary antibodies for 1 h, and stained with secondary antibodies for 1 h . Cells were washed with PBS containing 5% FBS between each step. Coverslips were exposed to 200 ng/mL 4′,6-diamidino-2-phenylindole (DAPI) (ThermoFisher Scientific, 62247) for 2 min to label nuclei, then mounted with ProLong Diamond Antifade Mountant (Invitrogen, P36961) and sealed with clear nail polish. For experiments requiring cytosolic signal quantification, HSC CellMask Green (Invitrogen, H32714) was added to coverslips at 2 μg/mL for 30 min, then washed several times in PBS, before DAPI staining. For Figure S2C, SYTOX (Invitrogen, MP33025) was added to

coverslips at 0.17 μM for 15 min, then washed in PBS. For Figure 1J, images were acquired on a LSM 780 confocal microscope (Zeiss) with a 40x oil-immersed objective and ZEN 3.3 software. For Figures 1F, 2C, 2E, 2G, S2C, S2E, 3A, 3K, 3M, S3C, S3G, S4H, 5F and 5G, images were acquired on an ECLIPSE Ti2 (Nikon) with a 60x oil-immersed objective and NIS-Elements AR 5.21.02 software. Representative images shown in Figures 1F, 2C, 2E, 2G, S2E, S3C, S4H, 5F and 5G were imported into Huygens Essential software (v21.4.0) and deconvolved using the 'aggressive' profile in the Deconvolution Express application. In Figures 3L, S3D and S3H, the nuclear cGAS intensity in each cell was quantified within the DAPI positive area, and cytosolic cGAS intensity per cell was quantified in the CellMask positive area minus the DAPI positive area (n   30 fields for each group from at least 3 biological replicates). In Figures 2D, 2F, 2H, S2F, S2G, S2H, 5H and S5C, the non-nuclear Z-DNA intensity per cell (cytoplasmic space including cytosol, mitochondria, and other organelles) was calculated from the whole cell area minus the DAPI positive area (n   20 or 30 fields for each group from at least 3 biological replicates). Z-DNA signals colocalizing with TOMM20 signals were quantified as mitochondrial Z-DNA, while the remaining non-nuclear Z-DNA staining was quantified as cytosolic Z-DNA. cGAS and Cellular Z-DNA intensity were quantified from Nikon .nd2 files using NIS-Elements AR 5.21.02.

Flow cytometry—The supernatants from cardiac isolations were centrifuged at $300 \times$ g, 4°C for 5 min with the centrifuge brake off to pellet the non-myocyte cells. The cell pellet was washed with $1 \times$ PBS containing 5% FBS, resuspended in $1 \times$ PBS with Fc Shield (TONBO, 70–0161-M001) and Ghost Dye Red 710 (TONBO, 13–0871-T100), and then loaded at 50 μL/well onto Laminar Wash Plates (Curiox, 96-DC-CL-05). The cells were left on ice for 25 min in dark to settle and then washed using Curiox Laminar Wash HT2000 system at the flow rate of 5 μL/s for 7 times. After wash, the cells were left in the wells with 25 μL of wash buffer. Antibodies were diluted in $1 \times$ PBS containing 5% FBS as $2 \times$ working solution, and 25 μL of the $2 \times$ antibodies were loaded into each well. The cells were incubated with antibodies on ice for 30 min in dark, and then wash as previously described for 12 times. After wash, the cells were collected in polystyrene round-bottom 12×75 mm tubes for flow cytometry analysis on Cytek® Aurora 5-Laser Spectral Cytometer.

Echocardiography—Mice were depilated at the chest area the day before echocardiography measurements. Anesthesia was induced by placing mice in a box with inhaled isoflurane at 2–3%. Afterwards, light anesthesia was maintained using a nose cone with inhaled isoflurane at 0.5–1%. Mice were immobilized on a heated stage, and continuous electric cardiogram (ECG), respiration, and temperature (via rectal probe) were monitored. Light anesthesia and core temperature were maintained to ensure near physiological status with heart rate at range of 470–520 beats per minute. Transthoracic echocardiography was performed using a VisualSonics Vevo 3100 system with a MX550D imaging transducer (center frequency of 40MHz). Parasternal long-axis (B-mode) and parasternal short-axis (M-mode) views of each animal were taken. Vevo LAB cardiac analysis package was used to analyze the data.

Histology—Mice were euthanized and tissues were washed in PBS and incubated for 24 h in 10% formalin and then transferred to 70% ethanol. Tissue embedding, sectioning, and staining were performed at AML Laboratories in St. Augustine, FL. Images of the H&E staining and Picrosirius red (P. Red) slides were acquired on ECLIPSE Ts2 (Nikon) with a 20x or 40x objective and NIS-Elements D 5.02.01 (Nikon) software. Blinded scoring of 9 independent fields of view from 6 hearts per genotype and treatment was performed to determine percent of cardiomyocytes exhibiting vacuolization post-Doxo. Collagen area was quantified using ImageJ.

Immunofluorescence staining in cardiac sections—Formalin-Fixed Paraffin-Embedded (FFPE) tissue sections were baked for 30 min, deparaffinized in xylene, and rehydrated by serial passage through graded concentrations of ethanol. Endogenous peroxidase in tissues was blocked with 0.9% H_2O_2/methanol for 40 min. Multiple (5) sequential heat-induced epitope retrieval (HIER) treatments were performed for 20 min each at 92–96°C in Citrate pH 6.0 buffer. After each HIER cycle in Citrate pH 6.0 buffer, sections were rinsed with diH$_2$O and cooled at RT for 20 min. Tissue sections were circled with hydrophobic barrier pens and blocked with 20% normal goat serum for 20 min before incubation with primary antibody for 20 min. Then, sections were rinsed with TBST for 10 min and incubated with HRP-conjugated secondary (A120–501P) for 20 min, followed by another 10 min rinse in TBST. Incubation with Opal fluorophore Opal690 was then done for 10 min, followed by a 10 min rinse in diH$_2$O. Bound primary and secondary antibodies were then subject to the next HIER treatment (as aforementioned) for 20 min. After staining with the Opal fluorophore, tissue specimens were stained with DAPI for 10 min and mounted in VECTASHIELD Vibrance Antifade Mounting Medium (ThermoFisher Scientific). Vectra Polaris Automated Quantitative Pathology Imaging System (Akoya Biosciences) was used for multispectral imaging at 40× magnification. Qupath[108] and ImageJ were used to export the images and to quantify the ATP5A1 fluorescence intensity.

RNA sequencing and bioinformatic analyses—Total cellular RNA from WT, *Tfam*^{+/−},*Zbp1*^{−/−} and *Tfam*^{+/−}*Zbp1*^{−/−} MEFs was prepared using Quick-RNA microprep kit (Zymo Research, R1051) and total cellular RNA from cardiomyocytes isolated from vehicle- and Doxo-treated mice was prepared using Direct-zol RNA miniprep kit (Zymo Research, R2052). Next-generation RNA sequencing procedure for both sets of samples were performed at Texas A&M University Bioinformatics Core. RNA sequencing data were analyzed using BaseSpace Sequence Hub (Illmina). In brief, STAR algorithm of RNAseq Alignment V2.0.0 software was utilized to align the results to reference genome Mus musculus/mm10 (RefSeq), then RNA-seq Differential Expression V1.0.0 software was used to obtain raw gene expression files and determine statistically significant changes in gene expression in *Tfam*^{+/−}, *Zbp1*^{−/−} and *Tfam*^{+/−}*Zbp1*^{−/−} MEFs relative to WT, or cardiomyocytes from Doxo-treated mice related to vehicle-treated mice. Heat maps were generated using GraphPad Prism. For Figures 5A and S5B, GSE40289 and GSE79413 datasets from the Gene Expression Omnibus (GEO) were analyzed using Gene Set Enrichment Analysis software (GSEA, Broad Institute)[109,110] to identify differentially regulated pathways, Set Comparison Appyter[111] and Enrichr[112–114] to identify the interactions between datasets and overlapping genes. For Figure 6B and 6D, RNA-seq

data from cardiomyocytes isolated from adult mouse hearts post Doxo challenge compared to vehicle controls were analyzed using ShinyGo[115] to generate the dot plots and GSEA to generate the enrichment plots.

QUANTIFICATION AND STATISTICAL ANALYSIS

Error bars displayed throughout the manuscript represent standard error of the mean (s.e.m.) and were calculated from triplicates unless otherwise indicated. For in vivo experiments, error bars were calculated from the average of triplicate technical replicates of at least 5 animals per point. For microscopy quantification, images were taken throughout the slide of each sample using the DAPI channel to avoid bias of selection. To reduce potential experimental bias, samples for cardiac function (EF, FS, IVS;s, LVID;s, LVPW;s, LVPW;d and LV mass) and histological analyses were blinded to researchers when performing analysis. The identities were only revealed at the final data analysis stage. No randomization or blinding was used for all other animal studies. No statistical method was used to predetermine sample size. Data shown are representative of at least 3 independent experiments, including microscopy images, western blots, gene expression analyses and all other cellular assays. All calculations of significance were determined using GraphPad Prism 9.5.0 software. The significance was determined by a p value of < 0.05, and annotated as $*P < 0.05$, $**P < 0.01$, and $***P < 0.001$.

Supplementary Material

Refer to Web version on PubMed Central for supplementary material.

ACKNOWLEDGEMENTS

INCLUSION AND DIVERSITY

We support inclusive, diverse, and equitable conduct of research.

REFERENCES

1. West AP, and Shadel GS (2017). Mitochondrial DNA in innate immune responses and inflammatory pathology. Nat. Rev. Immunol 17, 363–375. 10.1038/nri.2017.21. [PubMed: 28393922]

2. Riley JS, and Tait SW (2020). Mitochondrial DNA in inflammation and immunity. EMBO Rep. 21. 10.15252/embr.201949799.

3. Marchi S, Guilbaud E, Tait SWG, Yamazaki T, and Galluzzi L (2022). Mitochondrial control of inflammation. Nat. Rev. Immunol, 1–15. 10.1038/s41577-022-00760-x. [PubMed: 34799725]

4. Chen D, Tong J, Yang L, Wei L, Stolz DB, Yu J, Zhang J, and Zhang L (2018). PUMA amplifies necroptosis signaling by activating cytosolic DNA sensors. Proc. Natl. Acad. Sci 115, 3930–3935. 10.1073/pnas.1717190115. [PubMed: 29581256]

5. Szczesny B, Marcatti M, Ahmad A, Montalbano M, Brunyánszki A, Bibli S-I, Papapetropoulos A, and Szabo C (2018). Mitochondrial DNA damage and subsequent activation of Z-DNA binding protein 1 links oxidative stress to inflammation in epithelial cells. Sci. Rep 8, 914. 10.1038/s41598-018-19216-1. [PubMed: 29343810]

6. Saada J, McAuley RJ, Marcatti M, Tang TZ, Motamedi M, and Szczesny B (2022). Oxidative stress induces Z-DNA-binding protein 1–dependent activation of microglia via mtDNA released from retinal pigment epithelial cells. J. Biol. Chem 298. 10.1016/j.jbc.2021.101523.

7. Zhong F, Liang S, and Zhong Z (2019). Emerging Role of Mitochondrial DNA as a Major Driver of Inflammation and Disease Progression. Trends Immunol. 40, 1120–1133. 10.1016/j.it.2019.10.008. [PubMed: 31744765]

8. Lei Y, Martinez CG, Torres-Odio S, Bell SL, Birdwell CE, Bryant JD, Tong CW, Watson RO, West LC, and West AP (2021). Elevated type I interferon responses potentiate metabolic dysfunction, inflammation, and accelerated aging in mtDNA mutator mice. Sci. Adv 7, eabe7548. 10.1126/sciadv.abe7548. [PubMed: 34039599]

9. Menger KE, Rodríguez-Luis A, Chapman J, and Nicholls TJ (2021). Controlling the topology of mammalian mitochondrial DNA. Open Biol. 11, 210168. 10.1098/rsob.210168. [PubMed: 34547213]

10. Carvalho G, Repolês BM, Mendes I, and Wanrooij PH (2022). Mitochondrial DNA Instability in Mammalian Cells. Antioxid. Redox Signal 36, 885–905. 10.1089/ars.2021.0091. [PubMed: 34015960]

11. Pommier Y, Nussenzweig A, Takeda S, and Austin C (2022). Human topoisomerases and their roles in genome stability and organization. Nat. Rev. Mol. Cell Biol 23, 407–427. 10.1038/s41580-022-00452-3. [PubMed: 35228717]

12. Herbert A (2019). Z-DNA and Z-RNA in human disease. Commun. Biol 2, 1–10. 10.1038/s42003-018-0237-x. [PubMed: 30740537]

13. Ravichandran S, Subramani VK, and Kim KK (2019). Z-DNA in the genome: from structure to disease. Biophys. Rev 11, 383–387. 10.1007/s12551-019-00534-1. [PubMed: 31119604]

14. Maelfait J, Liverpool L, Bridgeman A, Ragan KB, Upton JW, and Rehwinkel J (2017). Sensing of viral and endogenous RNA by ZBP1/DAI induces necroptosis. EMBO J. 36, 2529–2543. 10.15252/embj.201796476. [PubMed: 28716805]

15. Jiao H, Wachsmuth L, Kumari S, Schwarzer R, Lin J, Eren RO, Fisher A, Lane R, Young GR, Kassiotis G, et al. (2020). Z-nucleic-acid sensing triggers ZBP1-dependent necroptosis and inflammation. Nature 580, 391–395. 10.1038/s41586-020-2129-8. [PubMed: 32296175]

16. Jiao H, Wachsmuth L, Wolf S, Lohmann J, Nagata M, Kaya GG, Oikonomou N, Kondylis V, Rogg M, Diebold M, et al. (2022). ADAR1 averts fatal type I interferon induction by ZBP1. Nature, 1–8. 10.1038/s41586-022-04878-9.

17. Guo H, Gilley RP, Fisher A, Lane R, Landsteiner VJ, Ragan KB, Dovey CM, Carette JE, Upton JW, Mocarski ES, et al. (2018). Species-independent contribution of ZBP1/DAI/DLM-1-triggered necroptosis in host defense against HSV1. Cell Death Dis. 9, 1–11. 10.1038/s41419-018-0868-3. [PubMed: 29298988]

18. Kuriakose T, Zheng M, Neale G, and Kanneganti T-D (2018). IRF1 Is a Transcriptional Regulator of ZBP1 Promoting NLRP3 Inflammasome Activation and Cell Death during Influenza Virus Infection. J. Immunol 10.4049/jimmunol.1701538.

19. Upton JW, Kaiser WJ, and Mocarski ES (2012). DAI/ZBP1/DLM-1 complexes with RIP3 to mediate virus-induced programmed necrosis that is targeted by murine cytomegalovirus vIRA. Cell Host Microbe 11, 290–297. 10.1016/j.chom.2012.01.016. [PubMed: 22423968]

20. Zhang T, Yin C, Boyd DF, Quarato G, Ingram JP, Shubina M, Ragan KB, Ishizuka T, Crawford JC, Tummers B, et al. (2020). Influenza Virus Z-RNAs Induce ZBP1-Mediated Necroptosis. Cell 180, 1115–1129.e13. 10.1016/j.cell.2020.02.050. [PubMed: 32200799]

21. Hubbard NW, Ames JM, Maurano M, Chu LH, Somfleth KY, Gokhale NS, Werner M, Snyder JM, Lichauco K, Savan R, et al. (2022). ADAR1 mutation causes ZBP1-dependent immunopathology. Nature, 1–7. 10.1038/s41586-022-04896-7.

22. de Reuver R, Verdonck S, Dierick E, Nemegeer J, Hessmann E, Ahmad S, Jans M, Blancke G, Van Nieuwerburgh F, Botzki A, et al. (2022). ADAR1 prevents autoinflammation by suppressing spontaneous ZBP1 activation. Nature, 1–6. 10.1038/s41586-022-04974-w.

23. Wallace KB, Sardão VA, and Oliveira PJ (2020). Mitochondrial Determinants of Doxorubicin-Induced Cardiomyopathy. Circ. Res 126, 926–941. 10.1161/CIRCRESAHA.119.314681. [PubMed: 32213135]

24. Bloom MW, Hamo CE, Cardinale D, Ky B, Nohria A, Baer L, Skopicki H, Lenihan DJ, Gheorghiade M, Lyon AR, et al. (2016). Cancer Therapy–Related Cardiac Dysfunction and Heart Failure. Circ. Heart Fail 9, e002661. 10.1161/CIRCHEARTFAILURE.115.002661. [PubMed: 26747861]

25. Lipshultz SE, Cochran TR, Franco VI, and Miller TL (2013). Treatment-related cardiotoxicity in survivors of childhood cancer. Nat. Rev. Clin. Oncol 10, 697–710. 10.1038/nrclinonc.2013.195. [PubMed: 24165948]

26. Mehta LS, Watson KE, Barac A, Beckie TM, Bittner V, Cruz-Flores S, Dent S, Kondapalli L, Ky B, Okwuosa T, et al. (2018). Cardiovascular Disease and Breast Cancer: Where These Entities Intersect: A Scientific Statement From the American Heart Association. Circulation 137, e30–e66. 10.1161/CIR.0000000000000556. [PubMed: 29437116]

27. Vejpongsa P, and Yeh ETH (2014). Prevention of anthracycline-induced cardiotoxicity: challenges and opportunities. J. Am. Coll. Cardiol 64, 938–945. 10.1016/j.jacc.2014.06.1167. [PubMed: 25169180]

28. Volkova M, and Russell R (2011). Anthracycline Cardiotoxicity: Prevalence, Pathogenesis and Treatment. Curr. Cardiol. Rev 7, 214–220. 10.2174/157340311799960645. [PubMed: 22758622]

29. Berthiaume JM, and Wallace KB (2007). Adriamycin-induced oxidative mitochondrial cardiotoxicity. Cell Biol. Toxicol 23, 15–25. 10.1007/s10565-006-0140-y. [PubMed: 17009097]

30. Zhou S, Palmeira CM, and Wallace KB (2001). Doxorubicin-induced persistent oxidative stress to cardiac myocytes. Toxicol. Lett 121, 151–157. 10.1016/s0378-4274(01)00329-0. [PubMed: 11369469]

31. Yen HC, Oberley TD, Gairola CG, Szweda LI, and St Clair DK (1999). Manganese superoxide dismutase protects mitochondrial complex I against adriamycin-induced cardiomyopathy in transgenic mice. Arch. Biochem. Biophys 362, 59–66. 10.1006/abbi.1998.1011. [PubMed: 9917329]

32. Carvalho FS, Burgeiro A, Garcia R, Moreno AJ, Carvalho RA, and Oliveira PJ (2014). Doxorubicin-induced cardiotoxicity: from bioenergetic failure and cell death to cardiomyopathy. Med. Res. Rev 34, 106–135. 10.1002/med.21280. [PubMed: 23494977]

33. Serrano J, Palmeira CM, Kuehl DW, and Wallace KB (1999). Cardioselective and cumulative oxidation of mitochondrial DNA following subchronic doxorubicin administration. Biochim. Biophys. Acta 1411, 201–205. 10.1016/s0005-2728(99)00011-0. [PubMed: 10216166]

34. Khiati S, Dalla Rosa I, Sourbier C, Ma X, Rao VA, Neckers LM, Zhang H, and Pommier Y (2014). Mitochondrial Topoisomerase I (Top1mt) Is a Novel Limiting Factor of Doxorubicin Cardiotoxicity. Clin. Cancer Res 20, 4873–4881. 10.1158/1078-0432.CCR-13-3373. [PubMed: 24714774]

35. Hangas A, Aasumets K, Kekäläinen NJ, Paloheinä M, Pohjoismäki JL, Gerhold JM, and Goffart S (2018). Ciprofloxacin impairs mitochondrial DNA replication initiation through inhibition of Topoisomerase 2. Nucleic Acids Res. 46, 9625–9636. 10.1093/nar/gky793. [PubMed: 30169847]

36. Wu Z, Oeck S, West AP, Mangalhara KC, Sainz AG, Newman LE, Zhang X-O, Wu L, Yan Q, Bosenberg M, et al. (2019). Mitochondrial DNA stress signalling protects the nuclear genome. Nat. Metab 1, 1209–1218. 10.1038/s42255-019-0150-8. [PubMed: 32395698]

37. Zhang Z, Meng P, Han Y, Shen C, Li B, Hakim MA, Zhang X, Lu Q, Rong M, and Lai R (2015). Mitochondrial DNA-LL-37 Complex Promotes Atherosclerosis by Escaping from Autophagic Recognition. Immunity 43, 1137–1147. 10.1016/j.immuni.2015.10.018. [PubMed: 26680206]

38. Oka T, Hikoso S, Yamaguchi O, Taneike M, Takeda T, Tamai T, Oyabu J, Murakawa T, Nakayama H, Nishida K, et al. (2012). Mitochondrial DNA that escapes from autophagy causes inflammation and heart failure. Nature 485, 251–255. 10.1038/nature10992. [PubMed: 22535248]

39. Nakayama H, and Otsu K (2018). Mitochondrial DNA as an inflammatory mediator in cardiovascular diseases. Biochem. J 475, 839–852. 10.1042/BCJ20170714. [PubMed: 29511093]

40. Cao DJ, Schiattarella GG, Villalobos E, Jiang N, May HI, Li T, Chen ZJ, Gillette TG, and Hill JA (2018). Cytosolic DNA Sensing Promotes Macrophage Transformation and Governs Myocardial Ischemic Injury. Circulation 137, 2613–2634. 10.1161/CIRCULATIONAHA.117.031046. [PubMed: 29437120]

41. King KR, Aguirre AD, Ye Y-X, Sun Y, Roh JD, Ng RP, Kohler RH, Arlauckas SP, Iwamoto Y, Savol A, et al. (2017). IRF3 and type I interferons fuel a fatal response to myocardial infarction. Nat. Med 23, 1481–1487. 10.1038/nm.4428. [PubMed: 29106401]

42. West AP, Khoury-Hanold W, Staron M, Tal MC, Pineda CM, Lang SM, Bestwick M, Duguay BA, Raimundo N, MacDuff DA, et al. (2015). Mitochondrial DNA stress primes the antiviral innate immune response. Nature 520, 553–557. 10.1038/nature14156. [PubMed: 25642965]

43. Pohjoismäki JLO, Wanrooij S, Hyvärinen AK, Goffart S, Holt IJ, Spelbrink JN, and Jacobs HT (2006). Alterations to the expression level of mitochondrial transcription factor A, TFAM, modify the mode of mitochondrial DNA replication in cultured human cells. Nucleic Acids Res. 34, 5815–5828. 10.1093/nar/gkl703. [PubMed: 17062618]

44. Nicholls TJ, Nadalutti CA, Motori E, Sommerville EW, Gorman GS, Basu S, Hoberg E, Turnbull DM, Chinnery PF, Larsson N-G, et al. (2018). Topoisomerase 3α Is Required for Decatenation and Segregation of Human mtDNA. Mol. Cell 69, 9–23.e6. 10.1016/j.molcel.2017.11.033. [PubMed: 29290614]

45. Menger KE, Chapman J, Díaz-Maldonado H, Khazeem MM, Deen D, Erdinc D, Casement JW, Di Leo V, Pyle A, Rodríguez-Luis A, et al. (2022). Two type I topoisomerases maintain DNA topology in human mitochondria. Nucleic Acids Res., gkac857. 10.1093/nar/gkac857.

46. Zhang H, Zhang Y-W, Yasukawa T, Dalla Rosa I, Khiati S, and Pommier Y (2014). Increased negative supercoiling of mtDNA in TOP1mt knockout mice and presence of topoisomerases IIα and IIβ in vertebrate mitochondria. Nucleic Acids Res. 42, 7259–7267. 10.1093/nar/gku384. [PubMed: 24803675]

47. Khatib IA, Deng J, Symes A, Kerr M, Zhang H, Huang SN, Pommier Y, Khan A, and Shutt TE (2022). Functional characterization of two variants of mitochondrial topoisomerase TOP1MT that impact regulation of the mitochondrial genome. J. Biol. Chem 298. 10.1016/j.jbc.2022.102420.

48. Ishii KJ, Kawagoe T, Koyama S, Matsui K, Kumar H, Kawai T, Uematsu S, Takeuchi O, Takeshita F, Coban C, et al. (2008). TANK-binding kinase-1 delineates innate and adaptive immune responses to DNA vaccines. Nature 451, 725–729. 10.1038/nature06537. [PubMed: 18256672]

49. Wang Z, Choi MK, Ban T, Yanai H, Negishi H, Lu Y, Tamura T, Takaoka A, Nishikura K, and Taniguchi T (2008). Regulation of innate immune responses by DAI (DLM-1/ZBP1) and other DNA-sensing molecules. Proc. Natl. Acad. Sci 105, 5477–5482. 10.1073/pnas.0801295105. [PubMed: 18375758]

50. Rongvaux A, Jackson R, Harman CCD, Li T, West AP, de Zoete MR, Wu Y, Yordy B, Lakhani SA, Kuan C-Y, et al. (2014). Apoptotic caspases prevent the induction of type I interferons by mitochondrial DNA. Cell 159, 1563–1577. 10.1016/j.cell.2014.11.037. [PubMed: 25525875]

51. Riley JS, Quarato G, Cloix C, Lopez J, O'Prey J, Pearson M, Chapman J, Sesaki H, Carlin LM, Passos JF, et al. (2018). Mitochondrial inner membrane permeabilisation enables mtDNA release during apoptosis. EMBO J. 37, e99238. 10.15252/embj.201899238. [PubMed: 30049712]

52. McArthur K, Whitehead LW, Heddleston JM, Li L, Padman BS, Oorschot V, Geoghegan ND, Chappaz S, Davidson S, Chin HS, et al. (2018). BAK/BAX macropores facilitate mitochondrial herniation and mtDNA efflux during apoptosis. Science 359. 10.1126/science.aao6047.

53. Zhang Y, Cui Y, An R, Liang X, Li Q, Wang H, Wang H, Fan Y, Dong P, Li J, et al. (2019). Topologically Constrained Formation of Stable Z-DNA from Normal Sequence under Physiological Conditions. J. Am. Chem. Soc 141, 7758–7764. 10.1021/jacs.8b13855. [PubMed: 30844265]

54. Möller A, Gabriels JE, Lafer EM, Nordheim A, Rich A, and Stollar BD (1982). Monoclonal antibodies recognize different parts of Z-DNA. J. Biol. Chem 257, 12081–12085. [PubMed: 7118931]

55. Buzzo JR, Devaraj A, Gloag ES, Jurcisek JA, Robledo-Avila F, Kesler T, Wilbanks K, Mashburn-Warren L, Balu S, Wickham J, et al. (2021). Z-form extracellular DNA is a structural component of the bacterial biofilm matrix. Cell 184, 5740–5758.e17. 10.1016/j.cell.2021.10.010. [PubMed: 34735796]

56. Schwartz T, Behlke J, Lowenhaupt K, Heinemann U, and Rich A (2001). Structure of the DLM-1–Z-DNA complex reveals a conserved family of Z-DNA-binding proteins. Nat. Struct. Biol 8, 761–765. 10.1038/nsb0901-761. [PubMed: 11524677]

57. Deigendesch N, Koch-Nolte F, and Rothenburg S (2006). ZBP1 subcellular localization and association with stress granules is controlled by its Z-DNA binding domains. Nucleic Acids Res. 34, 5007–5020. 10.1093/nar/gkl575. [PubMed: 16990255]

58. Ha SC, Van Quyen D, Hwang H-Y, Oh D-B, Brown BA, Lee SM, Park H-J, Ahn J-H, Kim KK, and Kim Y-G (2006). Biochemical characterization and preliminary X-ray crystallographic study of the domains of human ZBP1 bound to left-handed Z-DNA. Biochim. Biophys. Acta 1764, 320–323. 10.1016/j.bbapap.2005.12.012. [PubMed: 16448869]

59. Ha SC, Kim D, Hwang H-Y, Rich A, Kim Y-G, and Kim KK (2008). The crystal structure of the second Z-DNA binding domain of human DAI (ZBP1) in complex with Z-DNA reveals an unusual binding mode to Z-DNA. Proc. Natl. Acad. Sci 105, 20671–20676. 10.1073/pnas.0810463106. [PubMed: 19095800]

60. Thomas TJ, Seibold JR, Adams LE, and Hess EV (1993). Hydralazine induces Z-DNA conformation in a polynucleotide and elicits anti(Z-DNA) antibodies in treated patients. Biochem. J 294, 419–425. [PubMed: 8373356]

61. Timlin H, Wu M, Crespo-Bosque M, Geetha D, Ingolia A, Haque U, Towns MC, and Grader-Beck T (2019). Clinical Characteristics of Hydralazine-induced Lupus. Cureus 11, e4996. 10.7759/cureus.4996. [PubMed: 31497427]

62. Zhao B, Xu P, Rowlett CM, Jing T, Shinde O, Lei Y, West AP, Liu WR, and Li P (2020). The molecular basis of tight nuclear tethering and inactivation of cGAS. Nature 587, 673–677. 10.1038/s41586-020-2749-z. [PubMed: 32911481]

63. Volkman HE, Cambier S, Gray EE, and Stetson DB (2019). Tight nuclear tethering of cGAS is essential for preventing autoreactivity. eLife 8, e47491. 10.7554/eLife.47491. [PubMed: 31808743]

64. Zhang T, Yin C, Fedorov A, Qiao L, Bao H, Beknazarov N, Wang S, Gautam A, Williams RM, Crawford JC, et al. (2022). ADAR1 masks the cancer immunotherapeutic promise of ZBP1-driven necroptosis. Nature, 1–9. 10.1038/s41586-022-04753-7.

65. Ma Y, Wang X, Luo W, Xiao J, Song X, Wang Y, Shuai H, Ren Z, and Wang Y (2021). Roles of Emerging RNA-Binding Activity of cGAS in Innate Antiviral Response. Front. Immunol 12, 741599. 10.3389/fimmu.2021.741599. [PubMed: 34899698]

66. Wang D, Zhao H, Shen Y, and Chen Q (2022). A Variety of Nucleic Acid Species Are Sensed by cGAS, Implications for Its Diverse Functions. Front. Immunol 13. 10.3389/fimmu.2022.826880.

67. Slavik KM, Morehouse BR, Ragucci AE, Zhou W, Ai X, Chen Y, Li L, Wei Z, Bähre H, König M, et al. (2021). cGAS-like receptors sense RNA and control 3′2′-cGAMP signalling in Drosophila. Nature 597, 109–113. 10.1038/s41586-021-03743-5. [PubMed: 34261127]

68. Kesavardhana S, and Kanneganti T-D (2020). ZBP1: A STARGTE to decode the biology of Z-nucleic acids in disease. J. Exp. Med 217, e20200885. 10.1084/jem.20200885. [PubMed: 32584411]

69. Varinou L, Ramsauer K, Karaghiosoff M, Kolbe T, Pfeffer K, Müller M, and Decker T (2003). Phosphorylation of the Stat1 Transactivation Domain Is Required for Full-Fledged IFN-γ-Dependent Innate Immunity. Immunity 19, 793–802. 10.1016/S1074-7613(03)00322-4. [PubMed: 14670297]

70. Kovarik P, Stoiber D, Eyers PA, Menghini R, Neininger A, Gaestel M, Cohen P, and Decker T (1999). Stress-induced phosphorylation of STAT1 at Ser727 requires p38 mitogen-activated protein kinase whereas IFN-gamma uses a different signaling pathway. Proc. Natl. Acad. Sci. U. S. A 96, 13956–13961. 10.1073/pnas.96.24.13956. [PubMed: 10570180]

71. Staab J, Herrmann-Lingen C, and Meyer T (2013). CDK8 as the STAT1 serine 727 kinase? JAK-STAT 2, e24275. 10.4161/jkst.24275. [PubMed: 24069555]

72. Shutinoski B, Alturki NA, Rijal D, Bertin J, Gough PJ, Schlossmacher MG, and Sad S (2016). K45A mutation of RIPK1 results in poor necroptosis and cytokine signaling in macrophages, which impacts inflammatory responses in vivo. Cell Death Differ. 23, 1628–1637. 10.1038/cdd.2016.51. [PubMed: 27258786]

73. Sridharan H, Ragan KB, Guo H, Gilley RP, Landsteiner VJ, Kaiser WJ, and Upton JW (2017). Murine cytomegalovirus IE3-dependent transcription is required for DAI/ZBP1-mediated necroptosis. EMBO Rep. 18, 1429–1441. 10.15252/embr.201743947. [PubMed: 28607035]

74. Ingram JP, Thapa RJ, Fisher A, Tummers B, Zhang T, Yin C, Rodriguez DA, Guo H, Lane R, Williams R, et al. (2019). ZBP1/DAI Drives RIPK3-Mediated Cell Death Induced by IFNs in the Absence of RIPK1. J. Immunol 203, 1348–1355. 10.4049/jimmunol.1900216. [PubMed: 31358656]

75. Devos M, Tanghe G, Gilbert B, Dierick E, Verheirstraeten M, Nemegeer J, de Reuver R, Lefebvre S, De Munck J, Rehwinkel J, et al. (2020). Sensing of endogenous nucleic acids by ZBP1 induces keratinocyte necroptosis and skin inflammation. J. Exp. Med 217, e20191913. 10.1084/jem.20191913. [PubMed: 32315377]

76. Baik JY, Liu Z, Jiao D, Kwon H-J, Yan J, Kadigamuwa C, Choe M, Lake R, Kruhlak M, Tandon M, et al. (2021). ZBP1 not RIPK1 mediates tumor necroptosis in breast cancer. Nat. Commun 12, 1–14. 10.1038/s41467-021-23004-3. [PubMed: 33397941]

77. Yang Y, Wu M, Cao D, Yang C, Jin J, Wu L, Hong X, Li W, Lu L, Li J, et al. (2021). ZBP1-MLKL necroptotic signaling potentiates radiation-induced antitumor immunity via intratumoral STING pathway activation. Sci. Adv 7, eabf6290. 10.1126/sciadv.abf6290. [PubMed: 34613770]

78. Zhang S, Liu X, Bawa-Khalfe T, Lu L-S, Lyu YL, Liu LF, and Yeh ETH (2012). Identification of the molecular basis of doxorubicin-induced cardiotoxicity. Nat. Med 18, 1639–1642. 10.1038/nm.2919. [PubMed: 23104132]

79. Burridge PW, Li YF, Matsa E, Wu H, Ong S-G, Sharma A, Holmström A, Chang AC, Coronado MJ, Ebert AD, et al. (2016). Human induced pluripotent stem cell-derived cardiomyocytes recapitulate the predilection of breast cancer patients to doxorubicin-induced cardiotoxicity. Nat. Med 22, 547–556. 10.1038/nm.4087. [PubMed: 27089514]

80. Kuwata A, Ohashi M, Sugiyama M, Ueda R, and Dohi Y (2002). A case of reversible dilated cardiomyopathy after alpha-interferon therapy in a patient with renal cell carcinoma. Am. J. Med. Sci 324, 331–334. 10.1097/00000441-200212000-00008. [PubMed: 12495301]

81. Zimmerman S, Adkins D, Graham M, Petruska P, Bowers C, Vrahnos D, and Spitzer G (1994). Irreversible, severe congestive cardiomyopathy occurring in association with interferon alpha therapy. Cancer Biother. 9, 291–299. 10.1089/cbr.1994.9.291. [PubMed: 7719376]

82. Angulo MP, Navajas A, Galdeano JM, Astigarraga I, and Fernández-Teijeiro A (1999). Reversible cardiomyopathy secondary to alpha-interferon in an infant. Pediatr. Cardiol 20, 293–294. 10.1007/s002469900467. [PubMed: 10368457]

83. Khakoo AY, Halushka MK, Rame JE, Rodriguez ER, Kasper EK, and Judge DP (2005). Reversible cardiomyopathy caused by administration of interferon alpha. Nat. Clin. Pract. Cardiovasc. Med 2, 53–57. 10.1038/ncpcardio0069. [PubMed: 16265343]

84. Benjamini O, Kimhi O, and Lishner M (2007). Severe pleuropericarditis and cardiomyopathy induced by high dose interferon alpha-2b. Isr. Med. Assoc. J. IMAJ 9, 486–487. [PubMed: 17642403]

85. Zhao W, Ji F, Yu S, Li Z, and Deng H (2014). Dilated cardiomyopathy and hypothyroidism associated with pegylated interferon and ribavirin treatment for chronic hepatitis C: case report and literature review. Braz. J. Infect. Dis. Off. Publ. Braz. Soc. Infect. Dis 18, 110–113. 10.1016/j.bjid.2013.05.014.

86. Ackers-Johnson M, Li PY, Holmes AP, O'Brien S-M, Pavlovic D, and Foo RS (2016). A Simplified, Langendorff-Free Method for Concomitant Isolation of Viable Cardiac Myocytes and Nonmyocytes From the Adult Mouse Heart. Circ. Res 119, 909–920. 10.1161/CIRCRESAHA.116.309202. [PubMed: 27502479]

87. Feng J, Li Y, and Nie Y (2022). Methods of mouse cardiomyocyte isolation from postnatal heart. J. Mol. Cell. Cardiol 168, 35–43. 10.1016/j.yjmcc.2022.04.007. [PubMed: 35429553]

88. Uccellini MB, and García-Sastre A (2018). ISRE-Reporter Mouse Reveals High Basal and Induced Type I IFN Responses in Inflammatory Monocytes. Cell Rep. 25, 2784–2796.e3. 10.1016/j.celrep.2018.11.030. [PubMed: 30517866]

89. Pinto AR, Ilinykh A, Ivey MJ, Kuwabara JT, D'Antoni ML, Debuque R, Chandran A, Wang L, Arora K, Rosenthal N, et al. (2016). Revisiting Cardiac Cellular Composition. Circ. Res 118, 400–409. 10.1161/CIRCRESAHA.115.307778. [PubMed: 26635390]

90. Muller WA (2013). Getting Leukocytes to the Site of Inflammation. Vet. Pathol 50, 7–22. 10.1177/0300985812469883. [PubMed: 23345459]

91. Woodfin A, Voisin M-B, and Nourshargh S (2007). PECAM-1: A Multi-Functional Molecule in Inflammation and Vascular Biology. Arterioscler. Thromb. Vasc. Biol 27, 2514–2523. 10.1161/ATVBAHA.107.151456. [PubMed: 17872453]

92. Lafuse WP, Wozniak DJ, and Rajaram MVS (2020). Role of Cardiac Macrophages on Cardiac Inflammation, Fibrosis and Tissue Repair. Cells 10, 51. 10.3390/cells10010051. [PubMed: 33396359]

93. Dankort D, Curley DP, Cartlidge RA, Nelson B, Karnezis AN, Damsky WE, You MJ, DePinho RA, McMahon M, and Bosenberg M (2009). BRafV600E cooperates with Pten silencing to elicit metastatic melanoma. Nat. Genet 41, 544–552. 10.1038/ng.356. [PubMed: 19282848]

94. Damsky WE, Curley DP, Santhanakrishnan M, Rosenbaum LE, Platt JT, Gould Rothberg BE, Taketo MM, Dankort D, Rimm DL, McMahon M, et al. (2011). β-catenin signaling controls metastasis in Braf-activated Pten-deficient melanomas. Cancer Cell 20, 741–754. 10.1016/j.ccr.2011.10.030. [PubMed: 22172720]

95. Kaiser WJ, Upton JW, and Mocarski ES (2008). Receptor-Interacting Protein Homotypic Interaction Motif-Dependent Control of NF-κB Activation via the DNA-Dependent Activator of IFN Regulatory Factors1. J. Immunol 181, 6427–6434. 10.4049/jimmunol.181.9.6427. [PubMed: 18941233]

96. Kuriakose T, and Kanneganti T-D (2018). ZBP1: Innate Sensor Regulating Cell Death and Inflammation. Trends Immunol. 39, 123–134. 10.1016/j.it.2017.11.002. [PubMed: 29236673]

97. Daniels BP, Kofman SB, Smith JR, Norris GT, Snyder AG, Kolb JP, Gao X, Locasale JW, Martinez J, Gale M, et al. (2019). The Nucleotide Sensor ZBP1 and Kinase RIPK3 Induce the Enzyme IRG1 to Promote an Antiviral Metabolic State in Neurons. Immunity 50, 64–76.e4. 10.1016/j.immuni.2018.11.017. [PubMed: 30635240]

98. Peng R, Wang CK, Wang-Kan X, Idorn M, Kjær M, Zhou FY, Fiil BK, Timmermann F, Orozco SL, McCarthy J, et al. (2022). Human ZBP1 induces cell death-independent inflammatory signaling via RIPK3 and RIPK1. EMBO Rep. 23, e55839. 10.15252/embr.202255839. [PubMed: 36268590]

99. Rodriguez DA, Quarato G, Liedmann S, Tummers B, Zhang T, Guy C, Crawford JC, Palacios G, Pelletier S, Kalkavan H, et al. (2022). Caspase-8 and FADD prevent spontaneous ZBP1 expression and necroptosis. Proc. Natl. Acad. Sci 119, e2207240119. 10.1073/pnas.2207240119. [PubMed: 36191211]

100. Henriksen PA (2018). Anthracycline cardiotoxicity: an update on mechanisms, monitoring and prevention. Heart 104, 971–977. 10.1136/heartjnl-2017-312103. [PubMed: 29217634]

101. Chen H-J, Tas SW, and de Winther MPJ (2019). Type-I interferons in atherosclerosis. J. Exp. Med 217, e20190459. 10.1084/jem.20190459.

102. Shamseddine A, Patel SH, Chavez V, Moore ZR, Adnan M, Di Bona M, Li J, Dang CT, Ramanathan LV, Oeffinger KC, et al. (2022). Innate immune signaling drives late cardiac toxicity following DNA-damaging cancer therapies. J. Exp. Med 220, e20220809. 10.1084/jem.20220809. [PubMed: 36534085]

103. Xiao Z, Yu Z, Chen C, Chen R, and Su Y (2023). GAS-STING signaling plays an essential pathogenetic role in Doxorubicin-Induced Cardiotoxicity. BMC Pharmacol. Toxicol 24, 19. 10.1186/s40360-022-00631-0. [PubMed: 36964634]

104. Veatch JR, McMurray MA, Nelson ZW, and Gottschling DE (2009). Mitochondrial dysfunction leads to nuclear genome instability: A link through iron-sulfur clusters. Cell 137, 1247–1258. 10.1016/j.cell.2009.04.014. [PubMed: 19563757]

105. Hämäläinen RH, Landoni JC, Ahlqvist KJ, Goffart S, Ryytty S, Rahman MO, Brilhante V, Icay K, Hautaniemi S, Wang L, et al. (2019). Defects in mtDNA replication challenge nuclear genome stability through nucleotide depletion and provide a unifying mechanism for mouse progerias. Nat. Metab 1, 958–965. 10.1038/s42255-019-0120-1. [PubMed: 32694840]

106. Southern E (2006). Southern blotting. Nat. Protoc 1, 518–525. 10.1038/nprot.2006.73. [PubMed: 17406277]

107. Bryant JD, Lei Y, VanPortfliet JJ, Winters AD, and West AP (2022). Assessing Mitochondrial DNA Release into the Cytosol and Subsequent Activation of Innate Immune-related Pathways in Mammalian Cells. Curr. Protoc 2, e372. 10.1002/cpz1.372. [PubMed: 35175686]

108. Bankhead P, Loughrey MB, Fernández JA, Dombrowski Y, McArt DG, Dunne PD, McQuaid S, Gray RT, Murray LJ, Coleman HG, et al. (2017). QuPath: Open source software for digital pathology image analysis. Sci. Rep 7, 16878. 10.1038/s41598-017-17204-5. [PubMed: 29203879]

109. Subramanian A, Tamayo P, Mootha VK, Mukherjee S, Ebert BL, Gillette MA, Paulovich A, Pomeroy SL, Golub TR, Lander ES, et al. (2005). Gene set enrichment analysis: A knowledge-based approach for interpreting genome-wide expression profiles. Proc. Natl. Acad. Sci 102, 15545–15550. 10.1073/pnas.0506580102. [PubMed: 16199517]

110. Mootha VK, Lindgren CM, Eriksson K-F, Subramanian A, Sihag S, Lehar J, Puigserver P, Carlsson E, Ridderstråle M, Laurila E, et al. (2003). PGC-1α-responsive genes involved in oxidative phosphorylation are coordinately downregulated in human diabetes. Nat. Genet 34, 267–273. 10.1038/ng1180. [PubMed: 12808457]

111. Clarke DJB, Jeon M, Stein DJ, Moiseyev N, Kropiwnicki E, Dai C, Xie Z, Wojciechowicz ML, Litz S, Hom J, et al. (2021). Appyters: Turning Jupyter Notebooks into data-driven web apps. Patterns 2, 100213. 10.1016/j.patter.2021.100213. [PubMed: 33748796]

112. Chen EY, Tan CM, Kou Y, Duan Q, Wang Z, Meirelles GV, Clark NR, and Ma'ayan A (2013). Enrichr: interactive and collaborative HTML5 gene list enrichment analysis tool. BMC Bioinformatics 14, 128. 10.1186/1471-2105-14-128. [PubMed: 23586463]

113. Kuleshov MV, Jones MR, Rouillard AD, Fernandez NF, Duan Q, Wang Z, Koplev S, Jenkins SL, Jagodnik KM, Lachmann A, et al. (2016). Enrichr: a comprehensive gene set enrichment analysis web server 2016 update. Nucleic Acids Res. 44, W90–97. 10.1093/nar/gkw377. [PubMed: 27141961]

114. Xie Z, Bailey A, Kuleshov MV, Clarke DJB, Evangelista JE, Jenkins SL, Lachmann A, Wojciechowicz ML, Kropiwnicki E, Jagodnik KM, et al. (2021). Gene Set Knowledge Discovery with Enrichr. Curr. Protoc 1, e90. 10.1002/cpz1.90. [PubMed: 33780170]

115. Ge SX, Jung D, and Yao R (2020). ShinyGO: a graphical gene-set enrichment tool for animals and plants. Bioinformatics 36, 2628–2629. 10.1093/bioinformatics/btz931. [PubMed: 31882993]

116. Terenzi F, White C, Pal S, Williams BRG, and Sen GC (2007). Tissue-specific and inducer-specific differential induction of ISG56 and ISG54 in mice. J. Virol 81, 8656–8665. 10.1128/JVI.00322-07. [PubMed: 17553874]

117. Fensterl V, White CL, Yamashita M, and Sen GC (2008). Novel Characteristics of the Function and Induction of Murine p56 Family Proteins. J. Virol 82, 11045–11053. 10.1128/JVI.01593-08. [PubMed: 18768971]

Highlights

- Mitochondrial genome instability promotes Z-DNA formation

- ZBP1 stabilizes Z-DNA released from mitochondria to sustain IFN-I signaling

- A ZBP1-cGAS complex recruits RIPK1 and RIPK3 to augment STAT1 phosphorylation

- ZBP1 contributes to cardiac IFN-I responses and chemotherapy-related heart failure
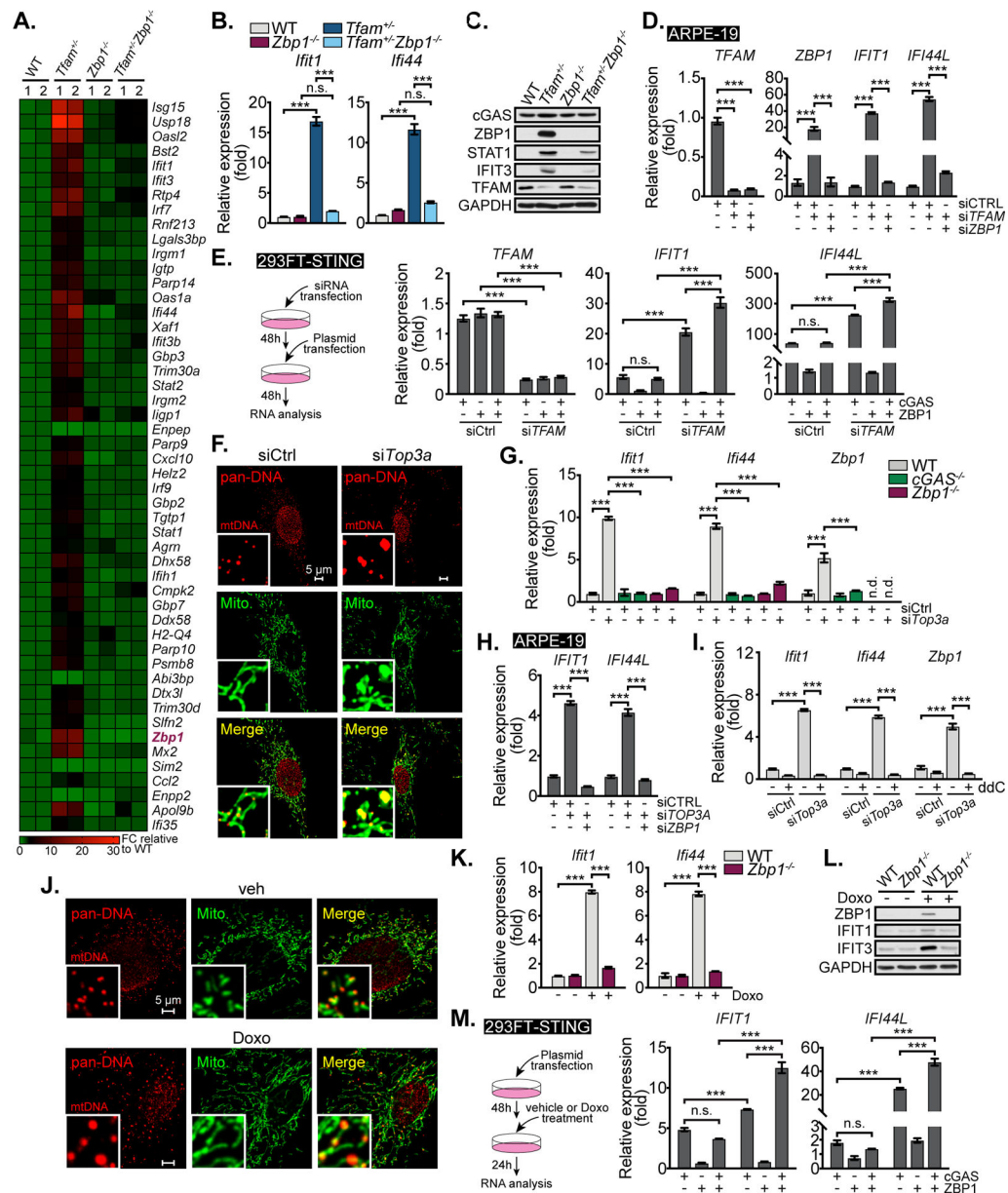
Figure 1. ZBP1 sustains IFN-I responses to mitochondrial genome instability.
A, RNA-seq heatmaps of top 50 genes with the lowest p-values between WT and *Tfam*$^{+/-}$ genotypes. Fold changes (FC) are normalized to the average of WT MEFs. **B, C,** qRT-PCR analysis (**B**) and western blots (**C**) of ISGs in WT, *Tfam*$^{+/-}$, *Zbp1*$^{-/-}$ and *Tfam*$^{+/-}$*Zbp1*$^{-/-}$ MEFs. **D,** qRT-PCR analysis in ARPE-19 transfected with indicated siRNAs for 72 h. **E,** Schematic illustration of siRNA and plasmid transfection in 293FT-STING (left). qRT-PCR analysis in 293FT-STING transfected with indicated siRNAs and plasmids (0.25 μg/mL cGAS or ZBP1) (right). **F,** Representative microscopy images of WT MEFs transfected with siCtrl or si*Top3a* and stained with anti-pan-DNA and -HSP60 (Mito.) antibodies. Inset panels are magnified 4x. **G,** qRT-PCR analysis in WT, *cGAS*$^{-/-}$ and *Zbp1*$^{-/-}$ MEFs transfected with siCtrl or si*Top3a* for 96 h. **H,** qRT-PCR analysis in ARPE-19 transfected

with indicated siRNAs for 72 h. **I.** qRT-PCR analysis in WT MEFs transfected with siCtrl or si*Top3a* with or without 2',3'-dideoxycytidine (ddC, 100 μM) for 72 h. **J,** Representative confocal microscopy images of WT MEFs treated with vehicle (veh) or Doxorubicin (Doxo, 500 nM, 24 h) and stained with anti-pan-DNA and -HSP60 (Mito.) antibodies. Inset panels are magnified 4x. **K, L,** qRT-PCR analysis (**K**) and western blots (**L**) of ISGs in WT and *Zbp1*$^{-/-}$ MEFs treated with or without Doxo (50 nM, 48 h). **M.** Schematic illustration of plasmid transfection and Doxo treatment in 293FT-STING (left). qRT-PCR analysis in 293FT-STING transfected with indicated plasmids (0.4 μg/mL cGAS or 0.8 μg/mL ZBP1) and with or without Doxo (200 nM) treatment (right). Statistical significance was determined using analysis of variance (ANOVA) and Tukey post hoc test (**A, D, E, G, H, I, L, M**). *$P < 0.05$, **$P < 0.01$, and ***$P < 0.001$. Error bars represent SEM. See also Figure S1 and Table S1.
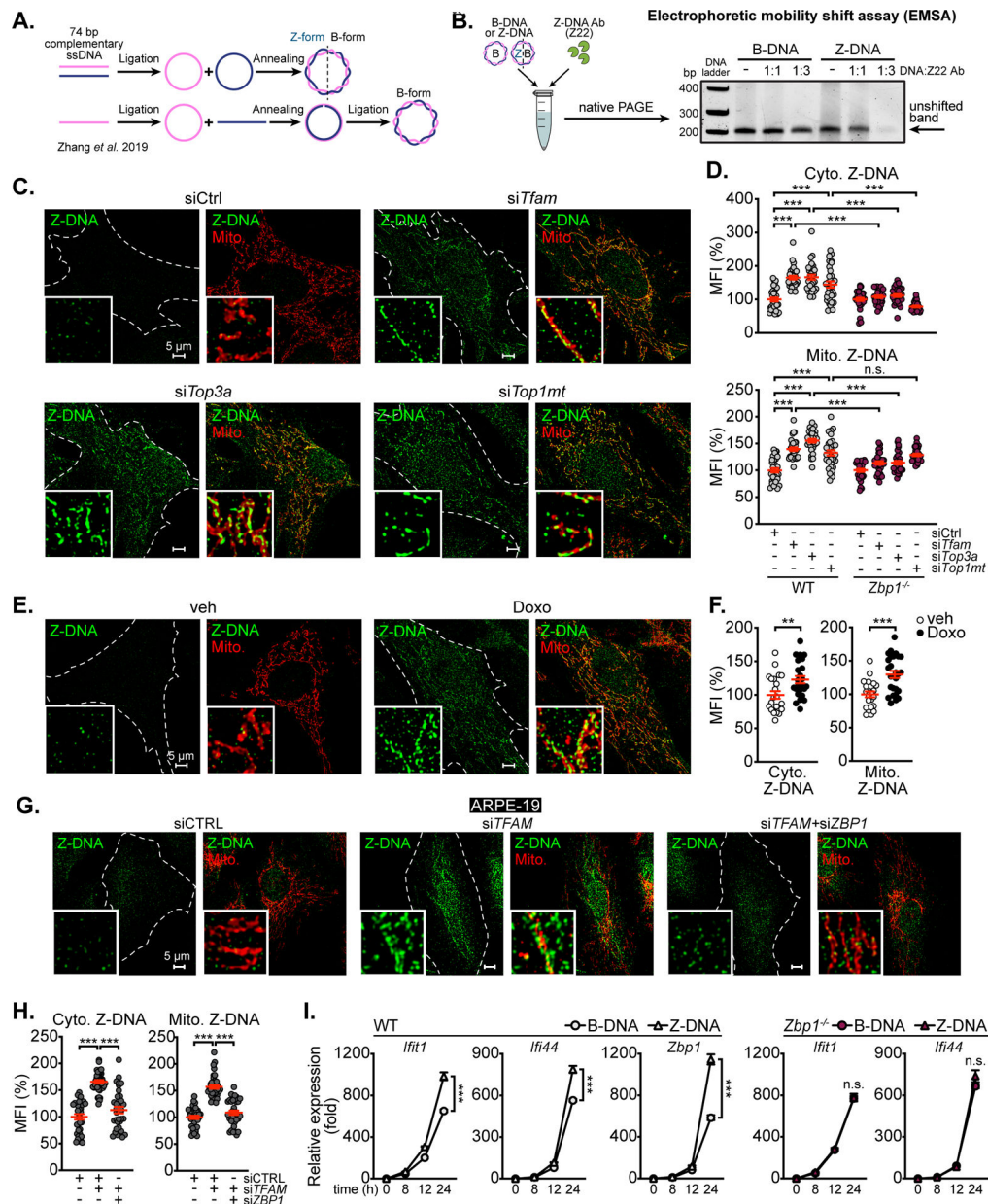
Figure 2. Mitochondrial genome instability promotes Z-form DNA accumulation that is stabilized by ZBP1.

A, Schematic illustration of circular Z-form and B-form DNA synthesis. **B,** Electrophoretic mobility shift assay (EMSA) measurement of binding of Z-DNA-specific antibody Z22 to B-DNA and Z-DNA. **C,** Representative images of WT MEFs transfected with indicated siRNAs for 72 h and stained with anti-Z-DNA and -TOMM20 (Mito.) antibodies. Inset panels are magnified 4x. **D,** Mean fluorescent intensity (MFI) quantification of cytosolic (Cyto.) and mitochondrial (Mito.) Z-DNA in WT and $Zbp1^{-/-}$ MEFs transfected with indicated siRNAs for 72 h. MFI percentiles are normalized to WT or $Zbp1^{-/-}$ MEFs transfected with siCtrl. **E, F,** Representative images of WT MEFs treated with veh or Doxo and stained with anti-Z-DNA and -TOMM20 antibodies (**E**). MFI of Cyto. and Mito. Z-DNA is quantified in (**F**). MFI percentiles are normalized to veh-treated WT MEFs. **G,**

H, Representative images of ARPE-19 transfected with indicated siRNAs for 72 h and stained with anti-Z-DNA and -TOMM20 antibodies (**G**). Inset panels are magnified 4x. MFI of Cyto. and Mito. Z-DNA is quantified in (**H**). MFI percentiles are normalized to ARPE-19 transfected with siCTRL. **I,** qRT-PCR analysis of ISGs in WT and *Zbp1*$^{-/-}$ MEFs transfected with B-DNA or Z-DNA (125 ng/mL) for indicated time. Statistical significance was determined using ANOVA (**D, I**) and Tukey post hoc test (**D**), or unpaired t-test (**F**). *P < 0.05, **P < 0.01, and ***P < 0.001. Error bars represent SEM. See also Figure S2.
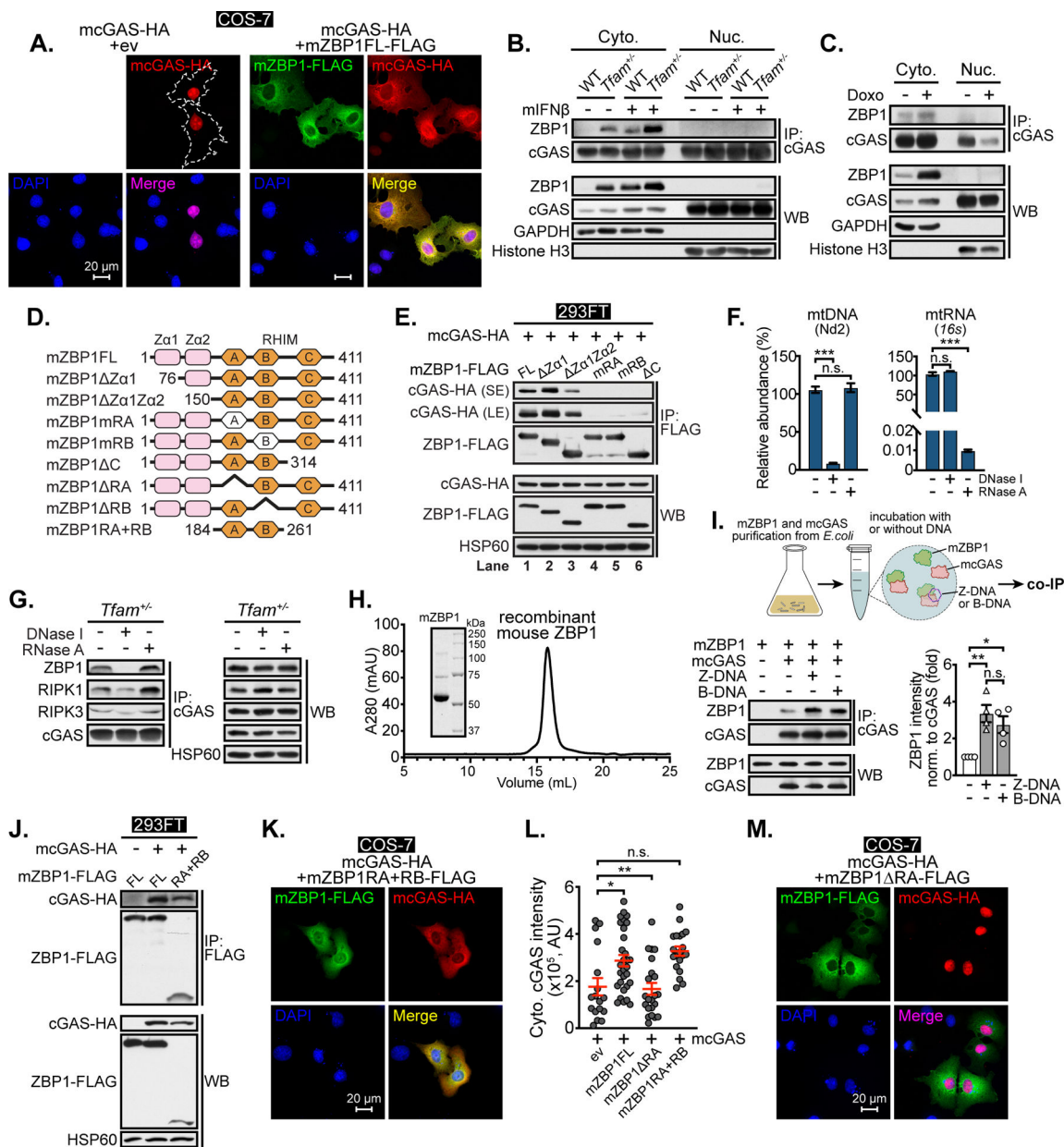
Figure 3. ZBP1 binds to cGAS in a DNA- and RHIM-dependent manner.
A, Representative images of COS-7 expressing indicated proteins and stained with anti-HA and -FLAG antibodies and DAPI (ev, empty vector). **B,** Endogenous cytosolic and nuclear co-immunoprecipitations (co-IP) in WT and *Tfam*^{+/−} MEFs with or without mouse IFNβ (mIFNβ) treatment (10 ng/mL, 6 h). **C,** Cytosolic and nuclear co-immunoprecipitation in WT MEFs treated with or without Doxo (50 nM, 48 h). **D,** Schematic representation of mouse ZBP1 full-length (mZBP1 FL), truncations and mutants. **E,** co-IP showing interactions between mouse cGAS (mcGAS) and mZBP1 FL, truncations or mutants in 293FT. SE, short exposure; LE, long exposure. **F,** qPCR analysis of mt-Nd2 (left) or qRT-PCR analysis of mt-*16s* (right) in cell lysates from G. **G,** Endogenous co-IP in *Tfam*^{+/−} MEFs with or without DNase I or RNase A treatment. **H,** Gel-filtration chromatography

and SDS–PAGE analyses of recombinant mZBP1 protein. **I,** Schematic illustration of co-IP between recombinant mcGAS and mZBP1 with or without DNA (top). co-IP showing interactions between mcGAS and mZBP1 with or without Z-DNA or B-DNA (bottom). Densitometry of ZBP1 in cGAS immunoprecipitates is shown in graph (n = 4). **J,** co-IP showing interactions between mcGAS and mZBP1 FL and RHIMA + RHIMB fragment (RA+RB) in 293FT. **K-M,** Representative images of COS-7 expressing indicated proteins and stained with anti-HA and -FLAG antibodies and DAPI (**K, M**). Cytosolic cGAS-HA intensity is quantified in (**L**). AU, arbitrary unit. Statistical significance was determined using ANOVA and Tukey post hoc test (**F, L**). *P < 0.05, **P < 0.01, and ***P < 0.001. Error bars represent SEM. See also Figure S3.
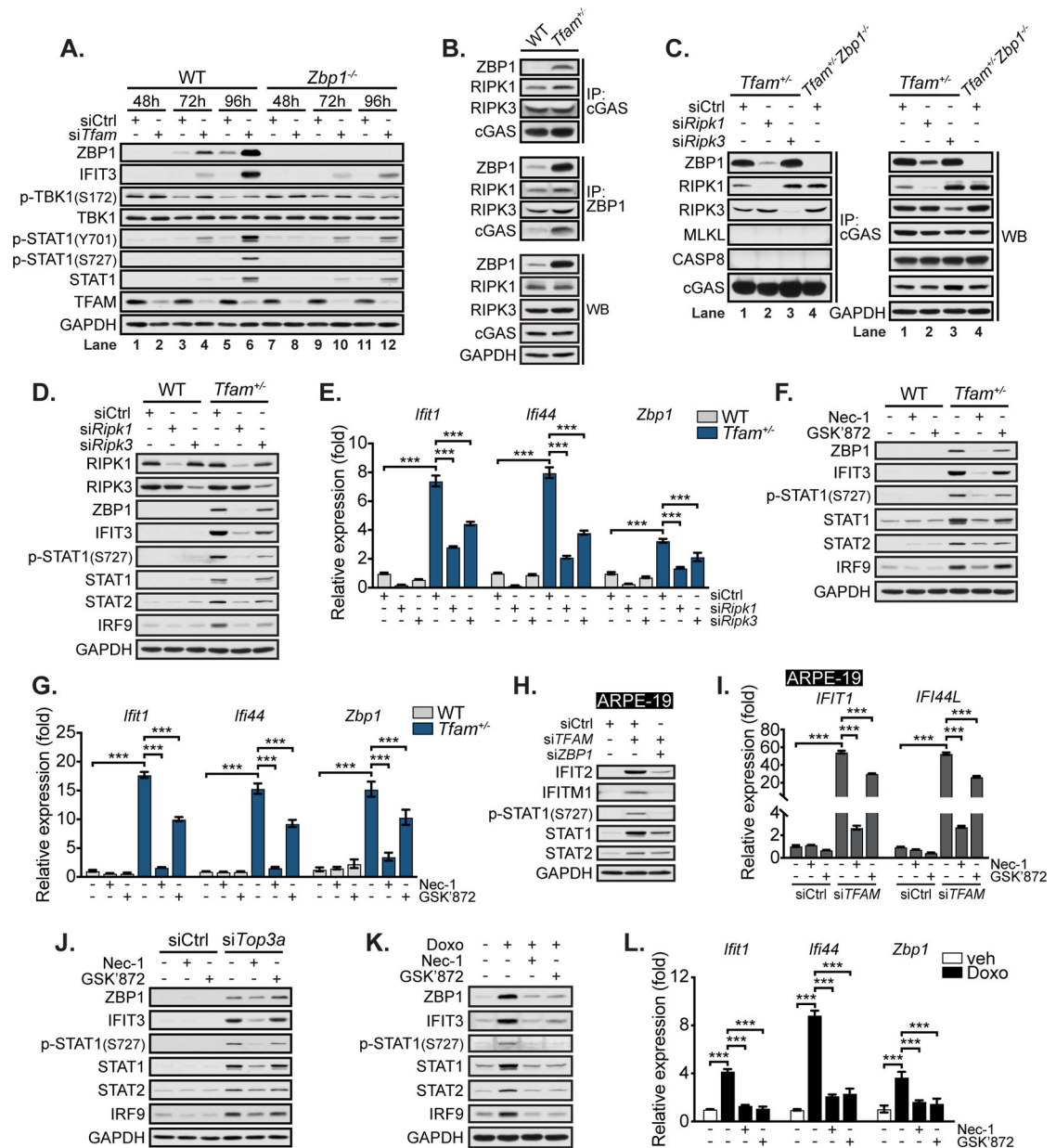
Figure 4. RIPK1 and RIPK3 localize to the ZBP1-cGAS complex and sustain IFN-I signaling to mitochondrial genome instability.

A, Western blots of WT and *Zbp1*^−/−^ MEFs transfected with siCtrl or si*Tfam* for indicated time. **B,** Endogenous co-IP in WT and *Tfam*^+/−^ MEFs. **C,** Endogenous co-IP in *Tfam*^+/−^ MEFs transfected with indicated siRNAs for 48 h and *Tfam*^+/−^*Zbp1*^−/−^ MEFs transfected with siCtrl for 48 h. **D, E,** Western blots (**D**) and qRT-PCR analysis (**E**) of WT and *Tfam*^+/−^ MEFs transfected with indicated siRNAs for 72 h. **F, G,** Western blots (**F**) and qRT-PCR analysis (**G**) of WT and *Tfam*^+/−^ MEFs treated with Necrostatin-1 (Nec-1, 10 μM) or GSK'872 (2.5 μM) for 48 h. **H,** Western blots of ARPE-19 transfected with indicated siRNAs for 72 h. **I,** qRT-PCR analysis in ARPE-19 transfected with siCTRL or si*TFAM* for 24 h and then treated with Nec-1 (100 μM) or GSK'872 (5 μM) for an additional 48 h.

J, Western blots of WT MEFs transfected with siCtrl or si*Top3a* for 48 h and then treated with Nec-1 (10 μM) or GSK'872 (2.5 μM) for an additional 48 h. **K, L,** Western blots (**K**) and qRT-PCR analysis (**L**) of WT MEFs treated with veh or Doxo (50 nM) for 24 h and then treated with Nec-1 (10 μM) or GSK'872 (2.5 μM) for an additional 24 h. Statistical significance was determined using ANOVA and Šídák (**E, G, I, L**). *$P < 0.05$, **$P < 0.01$, and ***$P < 0.001$. Error bars represent SEM. See also Figure S4.
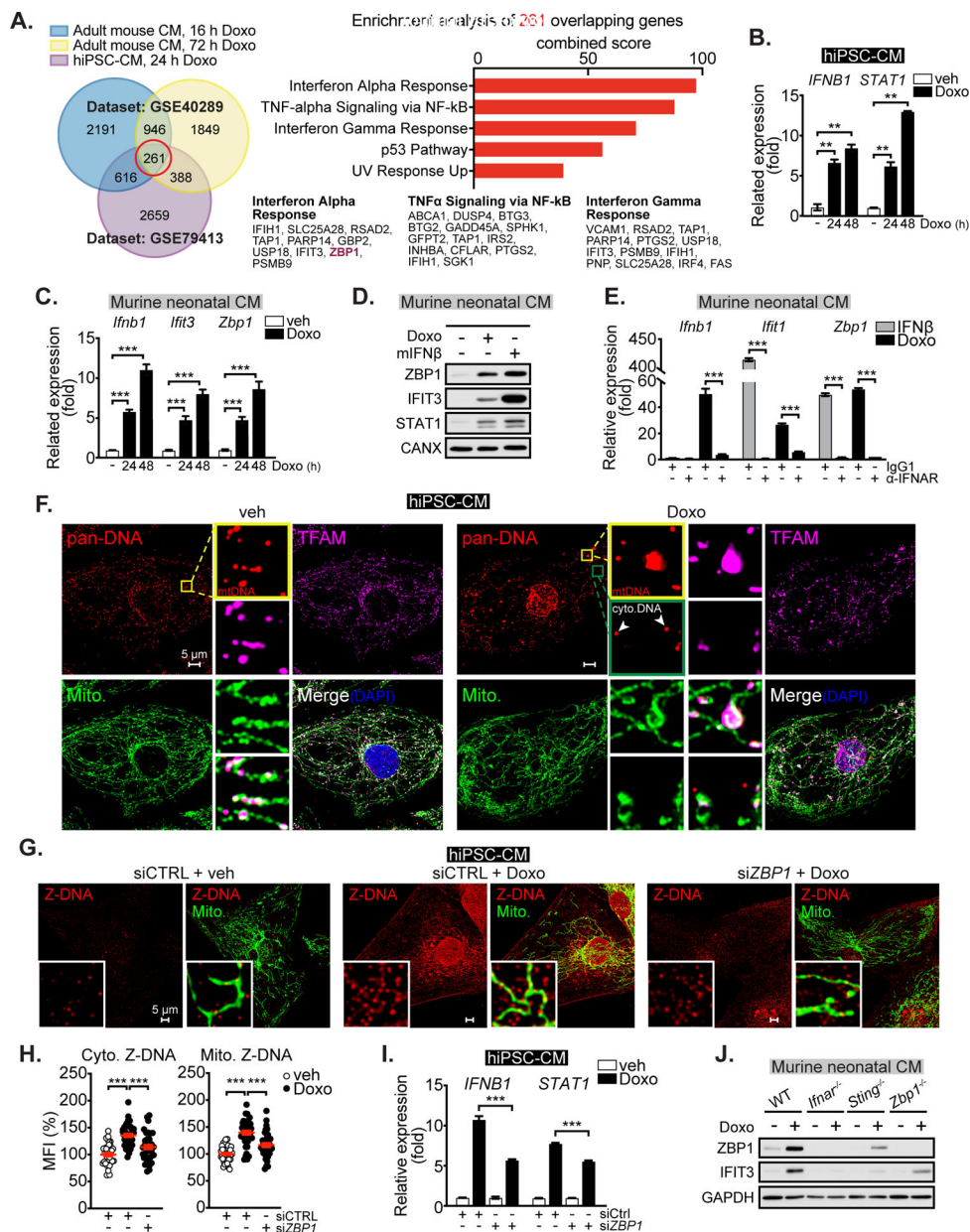
Figure 5. Doxorubicin induces mtDNA instability, mitochondrial Z-DNA accumulation, and IFN-I responses in cardiomyocytes.

A, Venn diagram of differentially expressed genes overlapping across datasets GSE40289 and GSE79413 (left). The top 5 pathways identified from the 261 commonly expressed genes from all three datasets (right). Shared gene lists from the top 3 pathways are shown (bottom). **B, C,** qRT-PCR analysis in veh or Doxo (250 nM) treated human induced pluripotent stem cell-derived cardiomyocytes (hiPSC-CM) (**B**) and murine neonatal CM (**C**). **D,** Western blots in Doxo (500 nM, 24h) or mouse IFNβ (mIFNβ, 1 ng/mL, 4 h) treated murine neonatal CMs. **E,** qRT-PCR analysis in anti-IgG1 or -interferon receptor 1 (α-IFNAR) antibody-blocked murine neonatal CMs exposed to mIFNβ or Doxo. CMs were pre-treated with anti-IgG1 or -IFNAR antibody at 15 μg/mL for 5 h before subjecting to mIFNβ (1 ng/mL, 4 h) or Doxo (500 nM, 24h) treatment. **F,** Representative images

of hiPSC-CMs treated with veh or Doxo and stained with anti-DNA, -TFAM and -PDH (Mito.) antibodies and DAPI. Inset panels are magnified 7x. **G, H,** Representative images of hiPSC-CMs transfected with siCTRL or si*ZBP1* for 48 h, treated with veh or Doxo (500 nM) for an additional 24 h and stained with anti-Z-DNA and -PDH antibodies (**G**). Inset panels are magnified 12x. MFI quantification of Cyto. and Mito. Z-DNA is quantified in (**H**). MFI percentiles are normalized to veh-treated hiPSC-CMs. **I,** qRT-PCR analysis in hiPSC-CMs transfected with siCTRL or si*ZBP1* for 24 h and then treated with veh or Doxo (250 nM) for an additional 48 h. **J,** Western blots in Doxo (500 nM, 24 h) treated WT, *Ifnar*$^{-/-}$, *Sting*$^{-/-}$ and *Zbp1*$^{-/-}$ murine neonatal CMs. Statistical significance was determined using unpaired t-test (**B, C, E**) or ANOVA and Tukey post hoc test (**H, I**). *P < 0.05, **P < 0.01, and ***P < 0.001. Error bars represent SEM. See also Figure S5.
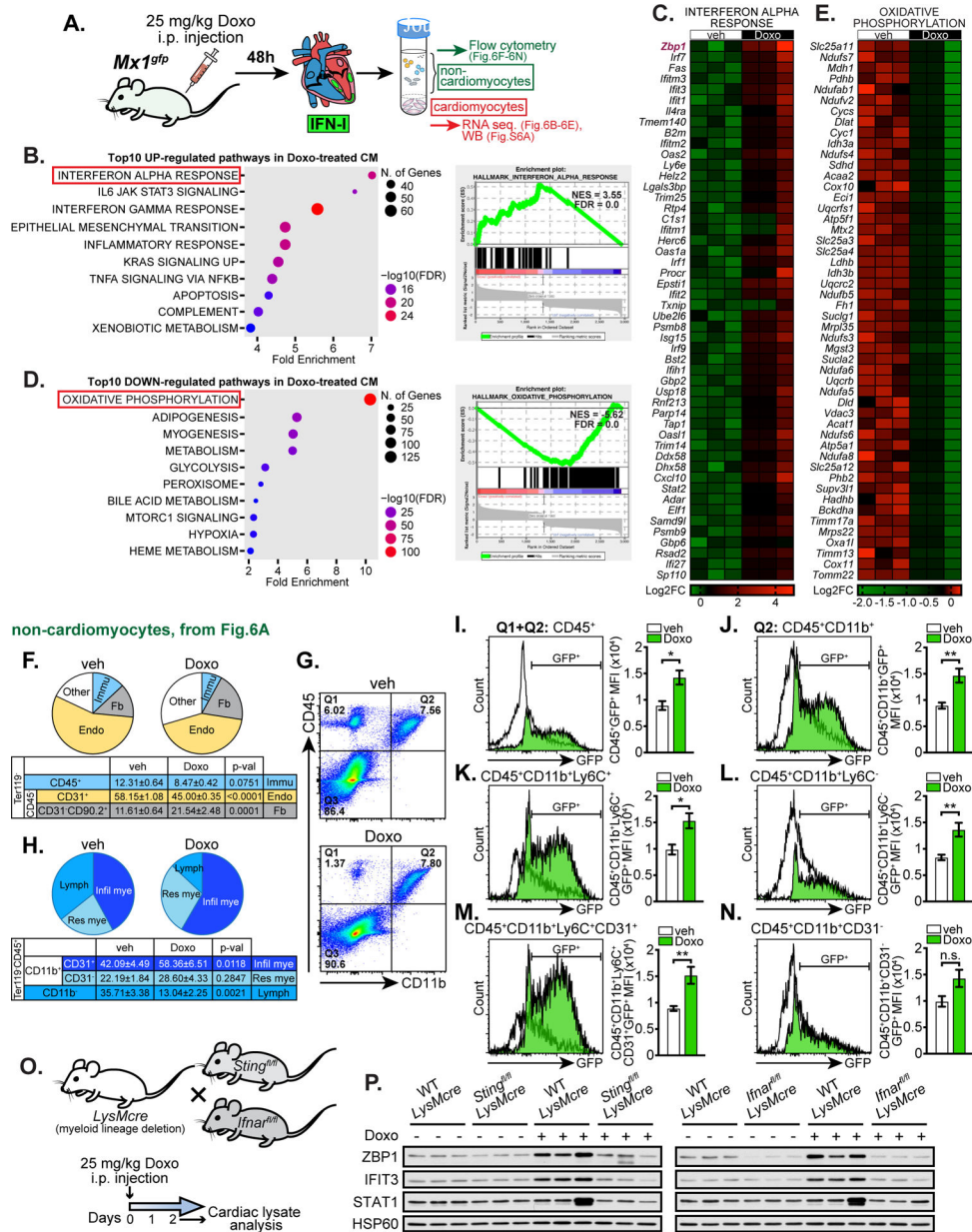
Figure 6. Doxorubicin induces ZBP1 and IFN-I responses in cardiomyocytes and cardiac myeloid cells in vivo.

A, Doxo i.p. challenge regimen, cardiac cell isolation and applications diagram. **B, D,** Pathway analysis of RNA-seq data from cardiomyocytes isolated from adult mouse hearts post Doxo challenge compared to veh controls. Dot plots (left) and enrichment plots (right) were generated from ShinyGo and Gene Set Enrichment Analysis (GSEA) software, respectively. NES = Normalized Enrichment Score, FDR = False Discovery Rate. **C, E,** Heatmaps of RNA-seq data displaying the top 50 up-regulated genes in interferon alpha response pathway (**C**) and top 50 down-regulated genes in oxidative phosphorylation pathway (**E**). Log2 fold changes (Log2FC) are normalized to the average of veh challenged CMs. **F,** Pie charts of major non-cardiomyocyte (non-CM) populations: immune cells (Immu), endothelial cells (Endo) and fibroblasts (Fb), compositions in veh and Doxo

challenged mouse hearts (n = 3 per treatment). **G,** Flow cytometric analysis of CD45 and CD11b on non-CM isolated from veh and Doxo challenged mouse hearts. **H,** Pie charts of major immune cell populations: infiltrating myeloid cells (Infil mye), resident myeloid cells (Res mye) and lymphocytes (Lymph), in veh and Doxo challenge mouse hearts (n = 4 per treatment). **I-N,** Flow cytometric analysis of Mx1^{gfp+} cells in indicated cardiac immune subpopulations. Histograms are representative of 4 independent experiments. MFI quantifications are shown on the right. **O,** Generation of myeloid-specific STING and IFNAR knockout mouse strains (top) and Doxo administration regimen (bottom). **P,** Western blots in cardiac lysates from WT*LysMcre*, *Sting*$^{fl/fl}$*LysMcre* and *Ifnar*$^{fl/fl}$*LysMcre* mice post veh or Doxo challenge (n = 3 per genotype per challenge). Statistical significance was determined using unpaired t-test (**I-N**). *P < 0.05, **P < 0.01, and ***P < 0.001. Error bars represent SEM. See also Figure S6 and Table S2.
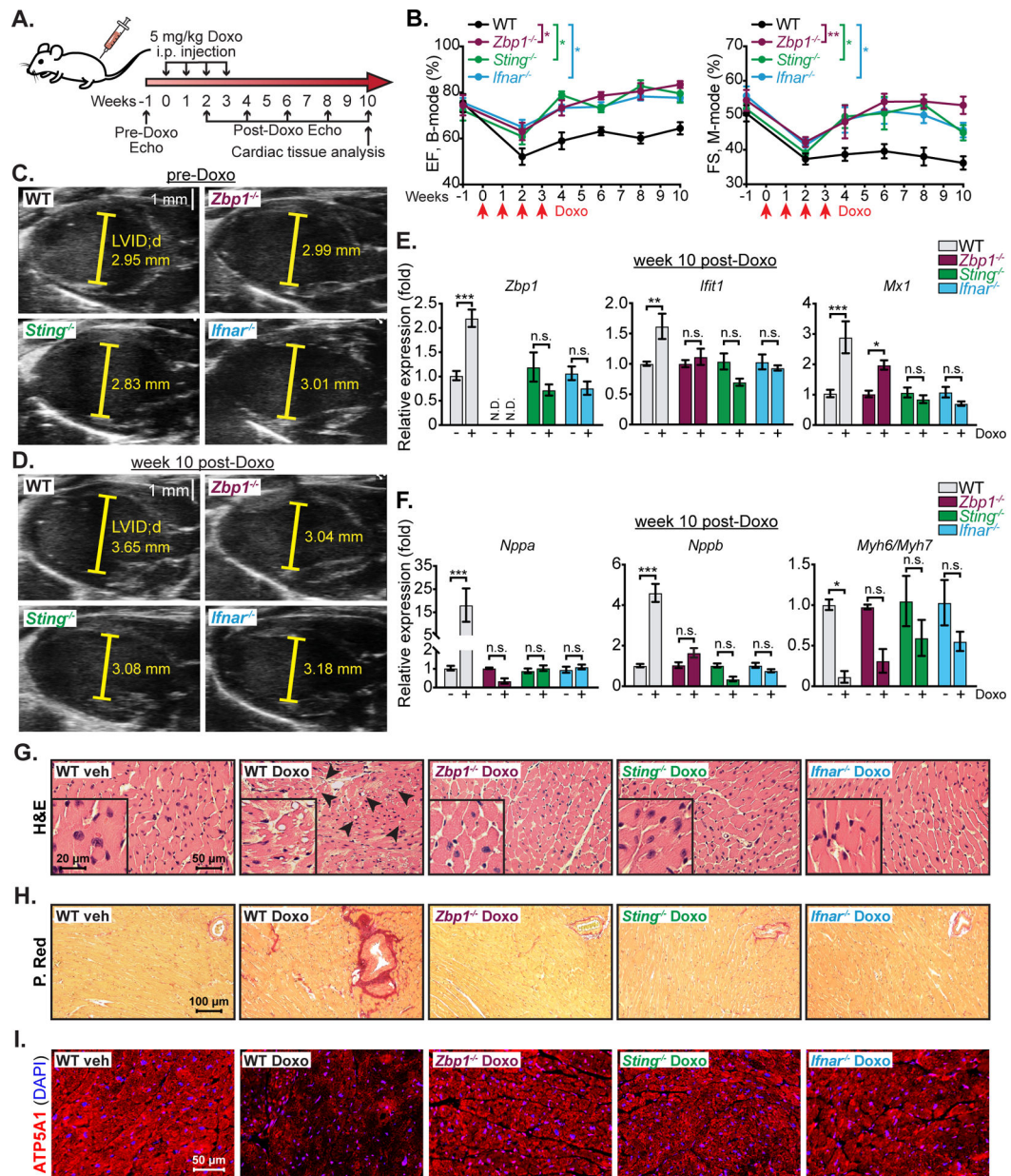
Figure 7. The ZBP1-IFN-I axis contributes to Doxorubicin-induced cardiac injury and cardiomyopathy.

A, Doxo i.p. challenge regimen, longitudinal cardiac monitoring, and cardiac harvest timepoint diagram. **B,** Left ventricular ejection fraction (EF) and fractional shortening (FS) calculated from B-mode or M-mode images (n = 6 per genotype). **C, D,** Representative parasternal long axis images from each genotype pre-Doxo (**C**) and at week 10 post Doxo challenge (**D**). **E, F,** qRT-PCR analysis of ISGs (**E**) or natriuretic peptides *Nppa*, *Nppb* and the *Myh6/7* expression ratio (**F**) in veh or Doxo treated WT, *Zbp1*$^{-/-}$, *Sting*$^{-/-}$ and *Ifnar*$^{-/-}$ cardiac lysates (n = 3 per genotype per treatment). **G-I,** Representative images of H&E staining (**G**), picrosirius red (P. Red) staining (**H**) and ATP5A1 and DAPI immunofluorescent staining (**I**) of the heart sections from veh treated WT mice and 10-week

post Doxo treated WT, *Zbp1*$^{-/-}$, *Sting*$^{-/-}$ and *Ifnar*$^{-/-}$ mice. Arrows in **G** indicate significant cardiomyocyte vacuolization in Doxo-treated WT heart section. Statistical significance was determined using ANOVA and Dunnett (**B**) or Šídák (**E, F**) post hoc test. *P < 0.05, **P < 0.01, and ***P < 0.001. Error bars represent SEM. See also Figure S7.

KEY RESOURCES TABLE

REAGENT or RESOURCE	SOURCE	IDENTIFIER
Antibodies		
IFIT1	Ganes Sen, Cleveland Clinic[116]	N/A
IFIT3	Ganes Sen, Cleveland Clinic[117]	N/A
cGAS	Cell Signaling Technology	31659
cGAS	Cell Signaling Technology	15102
IRF9	Cell Signaling Technology	28845
STAT1	Cell Signaling Technology	9172
p-STAT1 (Tyr701)	Cell Signaling Technology	7649
p-STAT1 (Ser727)	Cell Signaling Technology	9177
TBK1	Cell Signaling Technology	3504
p-TBK1	Cell Signaling Technology	5483
STAT2	Cell Signaling Technology	72604
CASP8	Cell Signaling Technology	4790
RIPK3	Cell Signaling Technology	95702
MLKL	Cell Signaling Technology	37705
GAPDH	Proteintech	60004–1
Histone H3	Proteintech	17168–1-AP
LMNB1	Proteintech	66095–1
HA	Proteintech	51064–2-AP
TFAM	Proteintech	22586–1-AP
IFIT2	Proteintech	12604-1-AP
IFITM1	Proteintech	60074–1-AP
CANX	Proteintech	10427–2-AP
TFAM	Millipore	ABE483
DNA	Millipore	CBL186
TOMM20	Millipore	MABT166
FLAG	Millipore	F1804
OXPHOS	Abcam	ab110413
PDH	Abcam	Ab110333
RIPK1	BD Biosciences	610458
BrdU	BD Biosciences	555627
ZBP1	Adipogen	AG-20B-0010-C100
HSP60	Santa Cruz Biotechinology	sc-1052
Z-DNA	Absolute	Ab00783–23.0
Z-DNA	Capralogics	P00008
MT-CO1	ThermoFisher Scientific	459600
NDUFA9	ThermoFisher Scientific	459100

REAGENT or RESOURCE	SOURCE	IDENTIFIER
NDUFS3	ThermoFisher Scientific	459130
CD45	BioLegend	103124
CD11b	BioLegend	101226
CD31	BioLegend	102418
Ter119	BioLegend	116210
CD90.2/ Thy1.2	BioLegend	105308
Ly6C	BioLegend	128049
ATP5A1	Fortis Life Sciences	A304–939A
*InVivo*Plus mouse IgG1 isotype control	Bio × Cell	BP0083
*InVivo*MAb anti-mouse IFNAR-1	Bio × Cell	BE0241
Anti-DYKDDDDK Tag (L5) Affinity Gel Antibody	Biolegend	651502
Chemicals, peptides, and recombinant proteins		
Doxorubicin	Selleck Chemicals	S1208
Hydralazine Hydrochloride	Spectrum	H1289
ISD	InvivoGen	tlrl-isdn
2'3'-cGAMP	InvivoGen	tlrl-nacga23–02
BrdU (5-Bromo-2´-Deoxyuridine)	Invitrogen	B23151
UltraPure™ Salmon Sperm DNA Solution	Invitrogen	15632011
ProLong Diamond Antifade Mountant	Invitrogen	P36961
HSC CellMask Green	Invitrogen	H32714
SYTOX® Green	Invitrogen	MP33025
Fetal Bovine Serum (FBS)	VWR	97068–085
Water, HyClone™ HyPure, Cell Culture Grade	VWR	82007–330
Dulbecco's Modified Eagle's Medium - high glucose	Sigma-Aldrich	D5796
Dulbecco's Phosphate Buffered Saline	Sigma-Aldrich	D8537
Polyinosinic–polycytidylic acid sodium salt	Sigma-Aldrich	P1530
ABT-737	Sigma-Aldrich	197333
Q-VD-OPh	Sigma-Aldrich	551476
Tamoxifen	Sigma-Aldrich	T5648
2',3'-Dideoxycytidine	Sigma-Aldrich	D5782
Polybrene Infection / Transfection Reagent	Sigma-Aldrich	TR-1003-G
cOmplete™, Mini, EDTA-free Protease Inhibitor Cocktail	Sigma-Aldrich	04693159001
Benzonase® Nuclease	Sigma-Aldrich	71205–3
Human IFN Alpha Hybrid Protein	PBL Assay Science	11200–1
Recombinant Human IFN-beta Protein	R&D Systems	8499-IF-010
Recombinant Mouse IFN-beta Protein	R&D Systems	8234-MB-010
Recombinant Mouse IFN-α	Biolegend	752806
Aphidicolin	Hello Bio	HB3690
4-Hydroxytamoxifen	Hello Bio	HB6040

REAGENT or RESOURCE	SOURCE	IDENTIFIER
Polyethylenimine (PEI)	Alfa Aesar	43896
Blasticidin S HCl	ThermoFisher Scientific	A1113903
Lipofectamine RNAiMAX reagent	ThermoFisher Scientific	13778150
T4 ligase	ThermoFisher Scientific	EL0011
Novex™ TBE Gels, 10%	ThermoFisher Scientific	EC6275BOX
4',6-diamidino-2-phenylindole (DAPI)	ThermoFisher Scientific	62247
Exonuclease I	ThermoFisher Scientific	720735KU
SYBR Green I Nucleic Acid Gel Stain	MedChemExpress	HY-K1004
Rabbit TrueBlot® Set	Rockland	88-1688-31
Mouse TrueBlot® Set	Rockland	88-7788-31
Pierce™ Control Agarose Resin	ThermoFisher Scientific	26150
DNase I	Worthington Biochemical	LS002139
RNase A	Worthington Biochemical	LS005650
PerfeCTa SYBR Green FastMix	Quanta	84069
Necrostatin-1	Selleckchem	S8037
GSK'872	Selleckchem	S8465
Blebbistatin	Selleckchem	S7099
Purified Anti-Mouse CD16 / CD32 (Fc Shield) (2.4G2)	TONBO	70–0161-M001
Ghost Dye™ Red 710	TONBO	13–0871-T100
Critical commercial assays		
E.Z.N.A.® plasmid DNA minikit	D6942–02	Omega bio-tek
Quick-RNA microprep kit	Zymo Research	R1051
Direct-zol RNA miniprep kit	Zymo Research	R2052
Micro BCA™ Protein Assay Kit	ThermoFisher Scientific	23235
Nuclear Complex Co-IP Kit	Active Motif	54001
2'3'-cGAMP ELISA Kit	Cayman	501700
LDH Cytotoxicity Detection Kit	TaKaRa	MK401
Neonatal Cardiomyocyte Isolation Kit	Miltenyi Biotec	130-098-373
Deposited data		
Raw and normalized count data from RNA-seq related to Table S1	This paper	GEO: GSE223553
Raw and normalized count data from RNA-seq related to Table S2	This paper	GEO: GSE223698
Mendeley dataset of additional confirmatory data not included in the paper	This paper	doi: 10.17632/cnw3htbbm9.2
Experimental models: Cell lines		
iCell Cardiomyocytes	FUJIFILM Cellular Dynamics	01434
293FT	Invitrogen	R70007
COS-7	ATCC	CRL-1651
ARPE-19	ATCC	CRL-2302

REAGENT or RESOURCE	SOURCE	IDENTIFIER
Platinum-A cells	Cell Biolabs	RV-102
WT MEF	This paper	N/A
Tfam$^{+/-}$ MEF	This paper	N/A
Zbp1$^{-/-}$ MEF	This paper	N/A
Tfam$^{+/-}$*Zbp1*$^{-/-}$ MEF	This paper	N/A
Experimental models: Organisms/strains		
C57BL/6J	The Jackson Laboratory	Strain # 000664
B6.129P2-*Lyz2*$^{tm1(cre)Ifo}$/J	The Jackson Laboratory	Strain # 004781
B6.FVB(129)-*A1cf*$^{Tg(Myh6-cre/Esr1*)1Jmk}$/J	The Jackson Laboratory	Strain # 005657
B6;SJL-*Sting1*$^{tm1.1Camb}$/J	The Jackson Laboratory	Strain # 031670
B6(Cg)-*Ifnar1*$^{tm1.1Ees}$/J	The Jackson Laboratory	Strain # 028256
B6.Cg-*Mx1*$^{tm1.1Agsa}$/J	The Jackson Laboratory	Strain # 033219
C57BL/6J-*Sting1*^{gt}/J	The Jackson Laboratory	Strain # 017537
B6.129S2-*Ifnar1*^{tm1Agt}/Mmjax	The Jackson Laboratory	MMRRC Strain #032045-JAX
B6;129-*Mavs*^{tm1Zjc}/J	The Jackson Laboratory	Strain # 008634
Tfam$^{+/-}$	West et al., 2015[42]	N/A
Zbp1$^{-/-}$	Ishii et al., 2008[48]	N/A
Sting$^{fl/fl}$ *LysMcre*	This paper	N/A
Ifnar$^{fl/fl}$ *LysMcre*	This paper	N/A
Sting$^{fl/fl}$ *αMHC-MerCreMer*	This paper	N/A
Ifnar$^{fl/fl}$ *αMHC-MerCreMer*	This paper	N/A
Oligonucleotides		
See Table S3	N/A	N/A
Recombinant DNA		
pUNO1-mSTINGwt-HA3x	InvivoGen	puno1ha-mstingwt
pUNO1-mCGAS-HA3x	InvivoGen	puno1ha-mcgas
pUNO1-hCGAS-HA3x	InvivoGen	puno1ha-hcgas
p3XFLAG-CMV-10-mZBP1 FL	Sridharan et al., 2017[73]	N/A
p3XFLAG-CMV-10-mZBP1 Zα1	Sridharan et al., 2017[73]	N/A
p3XFLAG-CMV-10-mZBP1 Zα1 Zα2	Sridharan et al., 2017[73]	N/A
p3XFLAG-CMV-10-mZBP1 mRHIMA	Sridharan et al., 2017[73]	N/A
p3XFLAG-CMV-10-mZBP1 mRHIMB	Sridharan et al., 2017[73]	N/A
p3XFLAG-CMV-10-mZBP1 C	Sridharan et al., 2017[73]	N/A
p3XFLAG-CMV-10-hZBP1 FL	Jason W. Upton, Auburn University	N/A
pMXs-IRES-Blast-mSTING-HIS	This paper	N/A
p3XFLAG-CMV-14-mZBP1 FL	This paper	N/A
p3XFLAG-CMV-14-mZBP1 RHIMA	This paper	N/A

REAGENT or RESOURCE	SOURCE	IDENTIFIER
p3XFLAG-CMV-14-mZBP1 RHIMB	This paper	N/A
p3XFLAG-CMV-14-mZBP1 RHIMA+B	This paper	N/A
pcDNA3.1-mCGAS FL-HA	This paper	N/A
pcDNA3.1-mCGAS N-term-HA	This paper	N/A
pcDNA3.1-mCGAS N-term -HA	This paper	N/A
pMXs-IRES-Blast-mSTING-HIS	This paper	N/A
Software and algorithms		
ZEN 3.3	Zeiss	N/A
NIS-Elements AR 5.21.02	Nikon	N/A
NIS-Elements D 5.02.01	Nikon	N/A
Huygens Essential 21.4.0	Scientific Volume Imaging	N/A
Vevo Lab 5.6.0	FUJIFILM VisualSonics	N/A
RNAseq Alignment V2.0.0	Illmina	N/A
RNA-seq Differential Expression V1.0.0	Illmina	N/A
Gene Set Enrichment Analysis software (GSEA) v4.2.3	Subramanian et al., 2005[109] and Mootha et al., 2003[110]	N/A
GraphPadPrism 9.5.0	GraphPad Software Inc.	N/A
ImageJ 1.8.0	NIH	N/A
FlowJo 10.8.2	BD Biosciences	N/A